climate

MDPI

Article

The Multi-Scale Dynamics Organizing a Favorable Environment for Convective Density Currents That Redirected the Yarnell Hill Fire

Michael L. Kaplan [1,*], Curtis N. James [1], Jan Ising [2], Mark R. Sinclair [1], Yuh-Lang Lin [2], Andrew Taylor [3], Justin Riley [2], Shak M. S. Karim [2] and Jackson Wiles [2]

[1] Department of Applied Aviation Sciences, Embry-Riddle Aeronautical University, Prescott, AZ 86301, USA; james61c@erau.edu (C.N.J.); sinclam@erau.edu (M.R.S.)
[2] Department of Physics and Applied Science and Technology, North Carolina A&T University, Greensboro, NC 27405, USA; jiising@aggies.ncat.edu (J.I.); ylin@ncat.edu (Y.-L.L.); jgriley@aggies.ncat.edu (J.R.); skarim@aggies.ncat.edu (S.M.S.K.); jtwiles@aggies.ncat.edu (J.W.)
[3] National Weather Service, National Oceanic and Atmospheric Administration, Central Illinois Forecast Office, Lincoln, IL 62656, USA; andrew.taylor@noaa.gov
* Correspondence: kaplanm1@erau.edu; Tel.: +1-(775)-300-8181

Abstract: The deadly shift of the Yarnell Hill, Arizona wildfire was associated with an environment exhibiting gusty wind patterns in response to organized convectively driven circulations. The observed synoptic (>2500 km) through meso-β (approximately 100 km) scale precursor environment that organized a mid-upper tropospheric cross-mountain mesoscale jet streak circulation and upslope thermally direct flow was examined. Numerical simulations and observations indicated that both circulations played a key role in focusing the upper-level divergence, ascent, downdraft potential, vertical wind shear favoring mobile convective gust fronts, and a microburst. This sequence was initiated at the synoptic scale by a cyclonic Rossby Wave Break (RWB) 72 h prior, followed by an anticyclonic RWB. These RWBs combined to produce a mid-continent baroclinic trough with two short waves ushering in cooler air with the amplifying polar jet. Cool air advection with the second trough and surface heating across the Intermountain West (IW) combined to increase the mesoscale pressure gradient, forcing a mid-upper tropospheric subsynoptic jet around the periphery of the upstream ridge over Southern Utah and Northern New Mexico. Convection was triggered by an unbalanced secondary jetlet circulation within the subsynoptic jet in association with a low-level upslope flow accompanying a mountain plains solenoidal circulation above the Mogollon Rim (MR) and downstream mountains.

Keywords: density current; Rossby Wave Break; jetlet; downdraft convective available potential energy; microburst; wildfire; ageostrophy

Citation: Kaplan, M.L.; James, C.N.; Ising, J.; Sinclair, M.R.; Lin, Y.-L.; Taylor, A.; Riley, J.; Karim, S.M.S.; Wiles, J. The Multi-Scale Dynamics Organizing a Favorable Environment for Convective Density Currents That Redirected the Yarnell Hill Fire. *Climate* **2021**, *9*, 170. https://doi.org/10.3390/cli9120170

Academic Editor: Salvatore Magazù

Received: 11 October 2021
Accepted: 19 November 2021
Published: 29 November 2021

1. Introduction

The Yarnell Hill Fire was a wildfire near Yarnell in Yavapai County, Arizona (note Figure 1a,b and Figure 3b for the regional Arizona topographic features surrounding Yarnell, Yarnell's location, and the local topography relative to the fire area at 0600 MST 1 July 2013). This wildfire was ignited by lightning on 28 June 2013. Late in the afternoon on 30 June, it overran and killed 19 City of Prescott firefighters, who were members of the Granite Mountain Hotshots. We will refer to this tragedy as the Yarnell Hill Fire Tragedy (YHFT). It was one of the deadliest wildfires in U.S. history [1] and the deadliest for firefighters since the 1933 Griffith Park fire in Los Angeles [2]. The YHFT fire front motion shifted from east–northeastward to southeastward to southward and, finally, southwestward over a brief period during the late afternoon of 30 June. The fire front shifts were consistent, with observed surface wind shifts and the estimated fire progression depicted in Figure 2a [3].

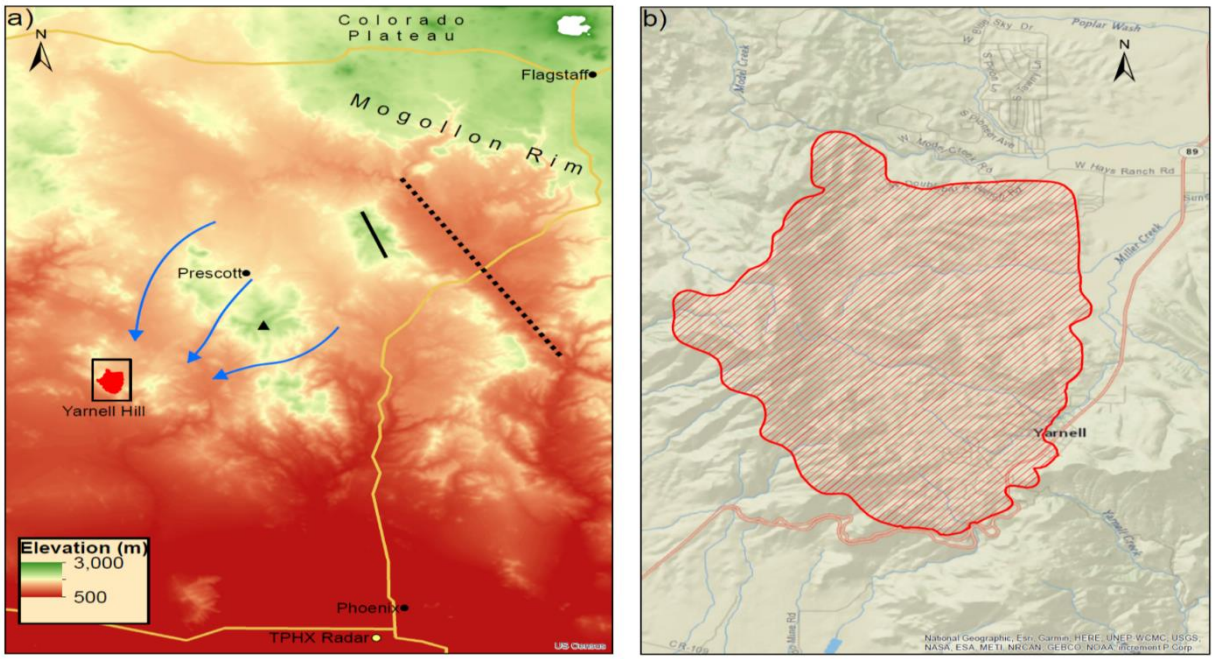

Figure 1. (**a**) Arizona topography, including an inset for Yarnell, as well as the locations of the Mogollon Rim, Black Hills (short solid line), Bradshaw Mountains (black triangle), Colorado Plateau, and Verde Valley (long dotted line). Blue streamlines indicate possible transects for airflow into Yarnell. (**b**) Topography surrounding Yarnell, including the Yarnell Hill fire perimeter in (**a**), at 0600 MST 1 July 2013 (note: light-red square inset on (**a**)).

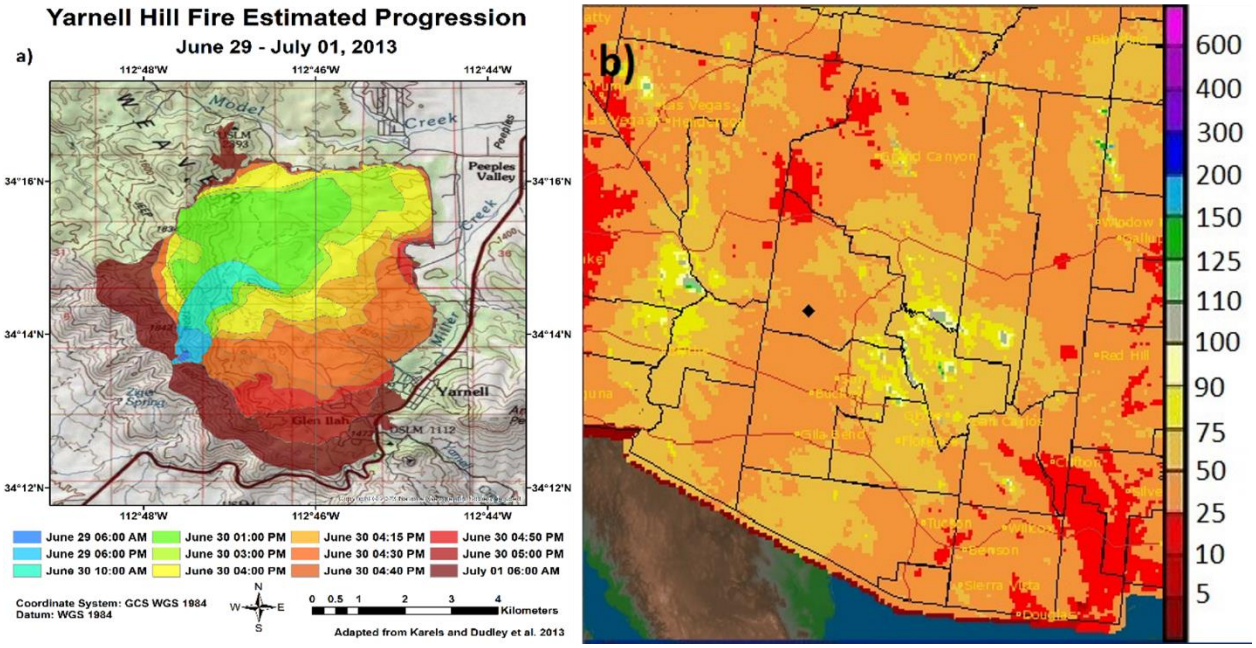

Figure 2. (**a**) Yarnell Hill fire progression during 0600 MST 29 June–0600 MST 1 July 2013 (from Karels and Dudley 2013) and (**b**) the percent of normal precipitation for parts of Arizona, New Mexico, and Southeastern California valid at 1357 UTC 2 July 2013 for the water year beginning on 1 October 2012 (Note: black diamond for Yarnell; NWS Flagstaff).

June 2013 was a remarkable month for weather in Arizona, the fourth-hottest June ever recorded up to that time. This also represented a period of prolonged drought in the Southwest U.S. The last week of June was the hottest week of what was to be a hot summer, with numerous daily high temperature records set for the 30th, e.g., 39 °C at Prescott (KPRC) located at approximately 1600 m above sea level (ASL) and approximately 60 km northeast

of Yarnell. Temperatures on 30 June approached and/or exceeded 38 °C at the Stanton and Peeples Valley Remote Atmospheric Weather Stations (RAWS) only a few kilometers from Yarnell (Office of the State Climatologist 2013: Summary of Conditions for June 2013, not shown). The Stanton and Peeples Valley RAWS both confirm a significant wind shift from the southwest and west to the north–northwest and north–northeast, respectively, close to the time of the YHFT between 1600 and 1700 MST (2300 and 0000 UTC). Figure 2b emphasizes the ongoing drought conditions in the southwest, particularly in Arizona at the beginning of July 2013. Most of the state was in a precipitation deficit approaching or even exceeding 50% for the 2013 water year, which began the previous October. Yarnell was in the middle of the 50–75% deficit region up to July 2nd for the 2013 water year, as depicted in Figure 2b, while Northwestern Arizona exceeded a 75% deficit. These observations, as well as others across the entire western and northern regions of the state, represented extreme drought conditions favorable for substantial diurnal surface sensible heating. This extreme heating is exemplified at Stanton, AZ, with an observation of 38 °C at 10:01 MST in response to a surface sensible heat flux of approximately 756 Wm^{-2} [4].

Yarnell is situated within a group of complex terrain features, including a local valley and a terrain gap. While Yarnell is situated in a narrow gap between low rolling hills (Figure 1b), much more extreme topography exists regionally to the east–northeast and immediate southwest (Figure 1a). To the east–northeast is a sequence of terrain features extending well above 2000 m MSL, including, sequentially, the Bradshaw Mountains, Black Hills, and Mogollon Rim (MR) (approximately 30, 75, and 150 km from Yarnell, respectively). Deep valleys exist between the Bradshaw Mountains and Black Hills, as well as between the Black Hills and MR, including Prescott Valley and Verde Valley, respectively. The Colorado Plateau (CP) is located to the northeast of the MR. Approximately 5 km to the immediate southwest of Yarnell, a sharp drop in topography approaching 1000 m in approximately 2 km separates the Western Arizona low desert region and Central Arizona's high semi-arid terrain. On the immediate western–northwestern and eastern sides of Yarnell are the Weaver Mountains. Hence, meteorological features propagating from a variety of directions would encounter substantial variability in the complex terrain elevation near Yarnell.

The convection associated with the YHFT occurred early in the summer. The National Weather Service (NWS) provided adequate forecasting support, and real-time forecasts of the event by the High-Resolution Rapid Refresh (HRRR) model were also generally representative of the weather hazards. Both indicated the possibility of gusty surface convective outflows [5]. The gusty surface winds could exacerbate wildfire danger in a dry hot region such as Central Arizona. Our research motivation is not to review the forecasts of the event but, rather, to understand in detail the larger-scale influences and downscale dynamical organizational processes causing the shifting gusty winds leading up to the YHFT.

Severe convection in Central Arizona has not been extensively analyzed in the literature with this goal in mind. One could separate this literature into three general categories: (1) in-depth observational climatologies of convective events, (2) regional simulations of seasonal climate and their relationship to the North American Monsoon (NAM), and (3) individual severe convective event observational analyses. The first category entails climatologies of severe convection and/or flooding rainfalls [6–8]. Most seminal is the study by Maddox et al. [6] that found three types of synoptic-scale environments favorable for severe weather in Central Arizona; however, they also pointed out that there is often ambiguity relating these environments to reliable real-time forecasting of severe weather. Furthermore, at the time of their climatological study, operational reanalyses were limited in scale to meso-α and greater, thus lacking mesoscale details critical in the complex geography of Central Arizona. The more contemporary and observationally comprehensive climatological studies of Mazon et al. [7] and Yang et al. [8] were largely focused on synoptic-scale predictive indices involving static stability, water vapor, and

geopotential height fields. Again, these represent broadscale predictive signals of large numbers of heavy rainfall or severe convective events without in-depth mesoscale details.

The second category involves employing regional simulation models to diagnose seasonal trends in the response of the NAM to forcing functions that control climate variability [9–11]. This type of study only deals with seasonal dynamical processes not individual case study multiscale processes. Finally, the third category, which has been quite rare, is that focusing on a single intense convective event [12,13]. McCollum et al. [12] analyzed the "surprise" 23 to 24 July 1990 Southwest Area Monsoon Project (SWAMP) extreme rainfall event in Phoenix, where few, if any, downscale dynamical linkages from the synoptic to mesoscales were unambiguously identified, given the lack of upper air observations. The surface and radar data were substantial and analyzed in depth but not high-resolution rawinsondes or numerical simulations. In another manuscript recently submitted on the Yarnell Hill Fire, Ising et al. [13] demonstrated how the general evolution of the key density current features from the MR to Yarnell were dependent on evaporational cooling, surface sensible heating, and the unique terrain structure near Yarnell. We will show some of these results in this manuscript as well, in so far as they support the density current evolution. Finally, there have been comprehensive studies of terrain-induced convection, such as those performed during the Cumulus Photogrammetic, In-situ, and Doppler Observations (CuPIDO) campaign in the Santa Catalina Mountains of Southeastern Arizona, as published in Damiani et al. [14] and Demko et al. [15]. These studies focus primarily on local convective initiation rather than severe convection resulting from downscale dynamical organizational processes. Analyses of downscale forcing in Central Arizona are relatively unique.

In this study, we will address this cascading multiscale set of processes with a focus on the meso-β scale and provide evidence that may aid in linking these circulations that provided an environment favorable for convective forcing near the YHFT. This study is presented with an understanding that the literature on density currents and multiscale convection is extraordinarily rich. The studies by Carbone et al. [16], Wakimoto [17], Rotunno et al. [18], Xu and Moncrieff [19], Liu and Moncrieff [20,21], Xue et al. [22], and Moncrieff and Liu [23], among others, supported the importance of significant alongstream vertical wind shears in the multicellular storms that generate long-lived gravity or density current outflows. Moncrief and Liu [23] performed numerical experiments indicating the importance of downshear forcing in producing density currents with deep ascent zones favorable for creating continuously regenerating convection. The focus of the study presented herein is intended to represent the synoptic-to-meso-β-scale components in the development of a paradigm of dynamical processes linking the planetary to the storm scale, including the generation of upper-level divergence, thermally direct upslope circulations, and low-level vertical shears at the meso-β scale, thus extending the previous research findings described above.

Section 2 of this manuscript represents a summary of the observational and numerically generated datasets used in the analysis. In Section 3.1, we will employ primarily synoptic and regional-scale observational analyses (synoptic-to-meso-α scale) to diagnose the precursor circulations that established a convectively favorable meso-β-scale environment. Section 3.2 will focus on the mass and momentum adjustments at the meso-β scale that led to ascent and vertical wind shear conducive to multiscale convection and density currents. Section 3.3 will depict the observed radar indicating the evolution of organized convection, as well as simulated wind perturbations in the PBL resulting from the convection. We will summarize our results in Section 4.

2. Methodology

We employed observational and numerically generated datasets in this study to describe the state of the synoptic-to-meso-β-scale atmosphere both over and upstream of Central Arizona to diagnose the environment favorable for the convectively forced wind systems responsible for the YHFT.

2.1. Observations

The following observational datasets were employed in the subsequent analyses: (1) Plymouth State Weather Center hourly surface meteograms [24], (2) European Centre for Medium Range Weather Forecasts ERA-Interim and ERA5 6-hourly and hourly upper-air analyses of dependent variables [25,26], (3) high-frequency radar control message datasets from the Plymouth State Weather Center archive [24], as well as high-resolution Doppler radar datasets and dual polarimetric radar datasets from the NOAA NIDS archive for the TPHX Doppler [27] and the Flagstaff, Arizona NWS Forecast Office [28], (4) soundings plotted from data downloaded from the NCEP NCEI (formerly NCDC) integrated global radiosonde archive [29], and (5) remote automatic weather station (RAWS) [30] surface data.

Synoptic-to-meso-β-scale maps were created using both ERA-Interim 0.75 × 0.75-degree resolution and ERA5 0.25 × 0.25-degree resolution reanalyses. The ERA-Interim reanalyses were employed to focus on synoptic-scale adjustments, including Rossby Wave Breaks (RWB) and the motion of the baroclinic short wave troughs. The finer details of the ERA5 were applied to understand the Central Arizona mass, momentum, temperature, and moisture evolution during the subsequent organization and evolution of convection. Soundings and ECMWF reanalysis data were plotted using Meteorological Analysis and Diagnosis Software (MADS) [31] on isobaric surfaces. For brevity, times and dates are hereafter formatted as HH/DD, two-digit hour/two–digit day of the month in Universal Coordinated Time (UTC).

2.2. Numerical Simulations

The nested grid numerical simulation employed Weather Research and Forecasting-ARW Version 4 (WRF-ARW) [32], as specified in [13]. Their simulations were employed in this manuscript to focus on the mesoscale jet adjustments and organizing circulations for convection and density current initiation and motion across the Black Hills, Bradshaw Mountains, and Weaver Mountains northeast of Yarnell. The numerical experiment consisted of three grids (Figure 3): a 7-km coarse and 2.33-km medium, as well as 777-m nested fine-scale mesh grids with one-way lateral boundary conditions. The 777-m grid was centered over Yarnell. The domain top was set at 50 hPa, with 50 stretched vertical levels most densely structured in the lower troposphere. The initial and D01 boundary condition data were derived from ERA5 with the lateral boundary conditions on the coarse mesh updated hourly. The grid nests employed lateral boundary conditions from the next coarser grid. D01 was run from 0000 UTC 30 June to 0000 UTC 1 July 2013, D02 was run from 1200 UTC 30 June to 0000 UTC 1 July 2013, and D03 wass run from 1500 UTC 30 June to 0000 UTC 1 July 2013, with data output for D03 every 15 min. The convective parameterization, the Grell-Freitas ensemble scheme [33], was applied in the 7-km simulation only, while the 2.33-km and 777-m domains explicitly resolved the moist convection. The other physics configurations were the same for all domains: the Purdue-Lin microphysical scheme [34], the Mellor–Yamada–Janjic (MYJ) planetary boundary layer (PBL) scheme [35–37], the Noah Land Surface Model [38,39], the Dudhia shortwave radiation scheme [40], and the RRTM longwave radiation scheme [41]. The figures depicting meteorological fields from the model simulation were created using the MetPy collection of tools for Python [42].

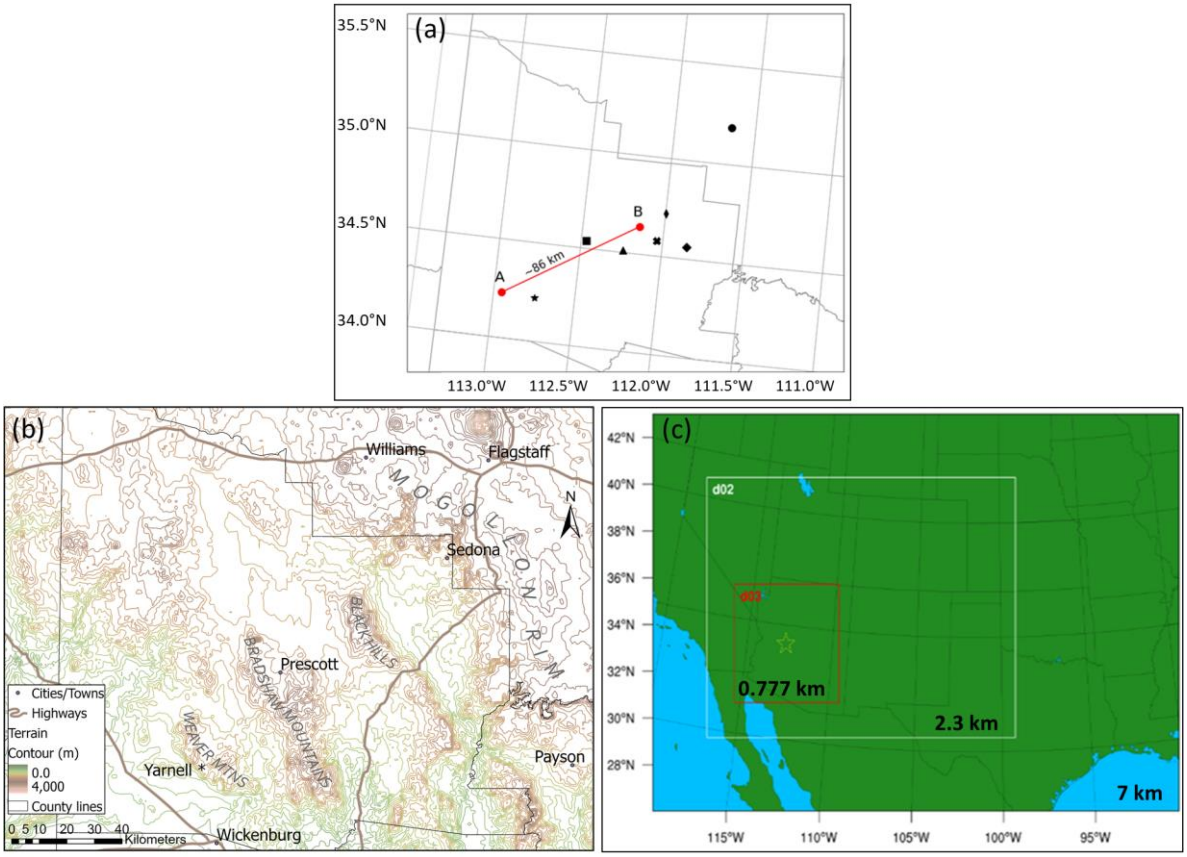

Figure 3. (**a**) Vertical cross-section between (A) Peeples Valley and (B) Black Hills of Central Arizona for WRF-ARW 777-m simulations only. (**b**) Map of Yavapai County and Southwestern Coconino County Arizona from Google Maps. Compare to Figure 1a. (**c**) WRF-ARW 7- km, 2.3-km, and 777-m grid domain setups. Each domain has a 3:1 grid ratio. The black and white stars represent the approximate location of Yarnell, AZ, while the black square = Prescott, black triangle = Dewey Humboldt, black X = Cherry, large black diamond = Camp Verde, small black diamond = Cottonw ood, and black circle = Flagstaff [13].

3. Results

3.1. Precursor Synoptic-to-Meso-α-Scale Dynamics

3.1.1. Continental RWB Resulting in trough Thinning

Figure 4 depicts the 12-hourly sequence of isobaric potential vorticity (PV) at 300 hPa, its horizontal advection, and the 300-hPa wind field across the lower 48 states and Southern Canada beginning approximately 96 h before the YHFT on 0000 UTC 27 June 2013 (abbreviated 00/27). Consistent with a cyclonic RWB within the upper tropospheric polar jet stream, a negatively tilted trough developed over the Great Lakes, as the first lobe of PV, propagates southeast during the 00/27–00/29 period. Cold air advection and adiabatic cooling accompanying cyclonic vorticity advection deepened this trough. Upstream, this process first elongated the ridge towards the east over the Intermountain West (IW) with the polar jet (PJ) maximum located southwest of the Great Lakes. The elongation of the ridge is the beginning of a process that restructures and relocates the center of the Four Corners high, which is typically located over the intersection of Arizona, Utah, Colorado, and New Mexico during the summer. Subsequently, the Four Corners high was elongated in a meridional direction, as it retrogresses towards the west. The troughing over the Great Lakes is consistent with trough thinning oriented northwest to southeast, as the first lobe of PV within the trough indicates the signal of meridional PV gradient reversal [43–45]. The PV gradient reversal is most pronounced just poleward of the Ohio River Valley across Michigan by 00/29 in Figure 4c. However, after 00/29, a second lobe of PV accompanying cold air advection propagated into the Central Plains and was associated with a shift in the structure of the ridge and anticyclonic flow much farther upstream over the IW

(Figure 3c–e). This shift reflected the elongation of the polar jet in the meridional direction and its movement upstream relative to the original cyclonic amplification of the trough 24–36 h earlier. This was followed by a gradual positive change in the tilt of the trough towards the north northeast. The PJ propagated more than 2000 km equatorward into Southern Mississippi. Most important for Central Arizona is the relocation of the polar jet's northwesterly flow and baroclinic zone upstream (westward) into the Central Rocky Mountains by 12/30. This second lobe of PV and its effect on the ridge structure after 00/30 can be described as a secondary RWB exhibiting anticyclonic characteristics.

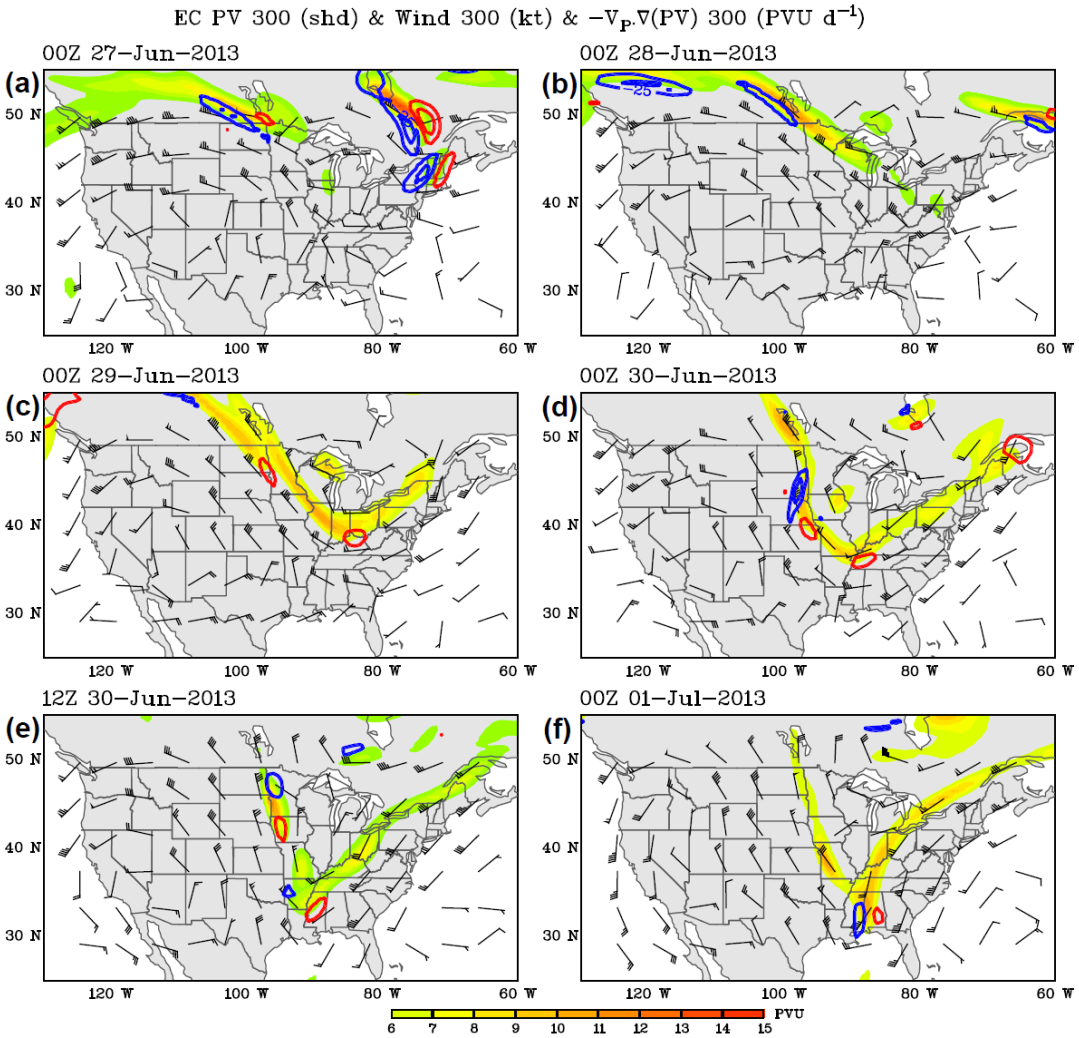

Figure 4. A 300-hPa ERA-Interim [25] potential vorticity (fill in PVU), PV advection (contoured >0 red and <0 blue in PVU d^{-1}), and 300-hPa wind vectors (black in m s^{-1}) valid at (**a**) 00/27, (**b**) 00/28, (**c**) 00/29, (**d**) 00/30, (**e**) 12/30, and (**f**) 00/01. These data analyses are original to this publication.

3.1.2. Dual Short Waves in Response to the Primary and Secondary RWB Leading to Subsequent IW Frontogenesis

In this section, we will outline how the synoptic-scale dynamics described in the previous subsection were focused downscale by the organization of two short-wave troughs and their subsequent cold frontogenesis. These dynamics act to concentrate mass and momentum perturbations along the western side of the Rocky Mountain Front Range that ultimately organize mid-upper tropospheric mesoscale jets. These adjustments were critical to creating the mid-upper tropospheric pressure gradient and eventual mesoscale jet/jetlet organization across the IW near the Four Corners region before 12/30.

The dual lobes of upper-tropospheric PV that evolved within the polar jet stream during the deepening and thinning of the upper-air trough first prior to 00/30 and then after 00/30, respectively, are both sequentially associated with these mid-lower tropospheric baroclinic short waves. Figure 5a,b and Figure 6a,b depict the 12-h evolution of the 700- and 850-hPa temperatures, wind, relative humidity, and height commencing at 06/30 and ending at 18/30 prior to the YHFT. At 06/30, short wave #1 (SW1) was in a transition zone between an upstream northwesterly flow and downstream southwesterly flow centered over the lower Mississippi River Valley. At the same time, short wave #2 (SW2) was in a transition zone between the upstream north–northeasterly flow and downstream west–northwesterly flow centered over the Northern Great Plains. Both waves exhibited confluent flow and horizontally nonuniform cold air advection below 300 hPa consistent with cold frontogenesis. They represented the lower tropospheric reflection of the dual lobes of PV in Figure 4e,f that have developed and propagated into lower Mississippi River Valley first during trough thinning accompanying the primary cyclonic RWB and, subsequently, with the secondary anticyclonic RWB. However, the most confluent flow resulting in zonal temperature, wind, and relative humidity gradients, particularly at 850 hPa, existed where the far western periphery of both SW1 and SW2 interface with the Front Range of the Rocky Mountains.

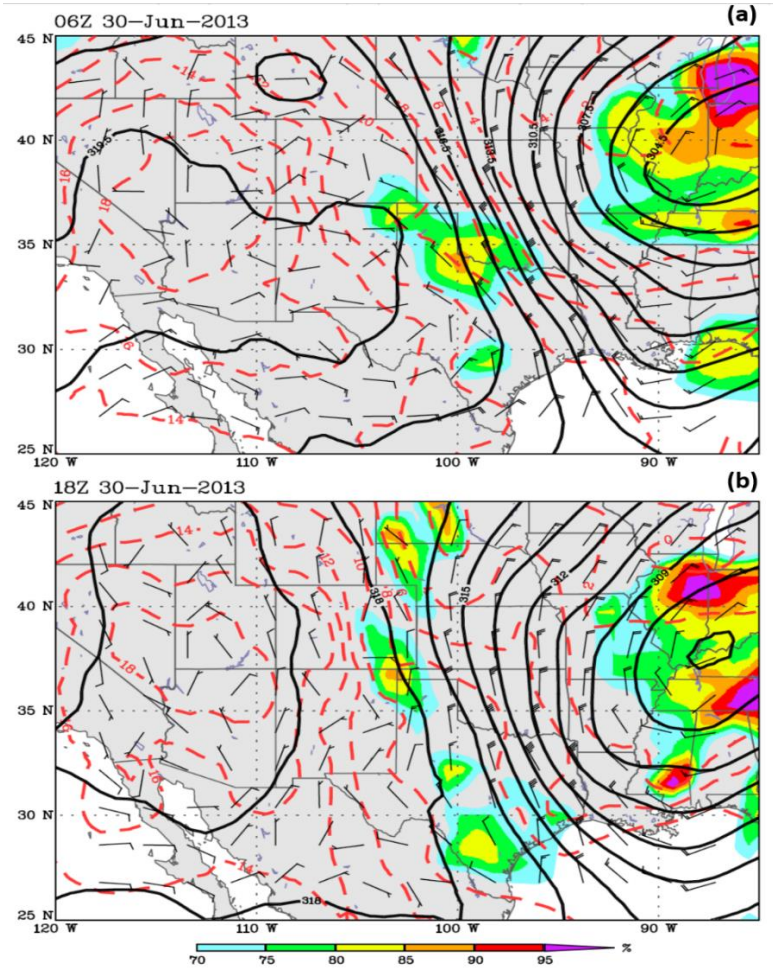

Figure 5. ERA-Interim [25] 700-hPa height (solid in m), temperature (red dashed in °C), wind barbs in kt, and 700-hPa mean relative humidity (fill in %) valid at (**a**) 0600 UTC and (**b**) 1800 UTC 30 June 2013. These data analyses are original to this publication.

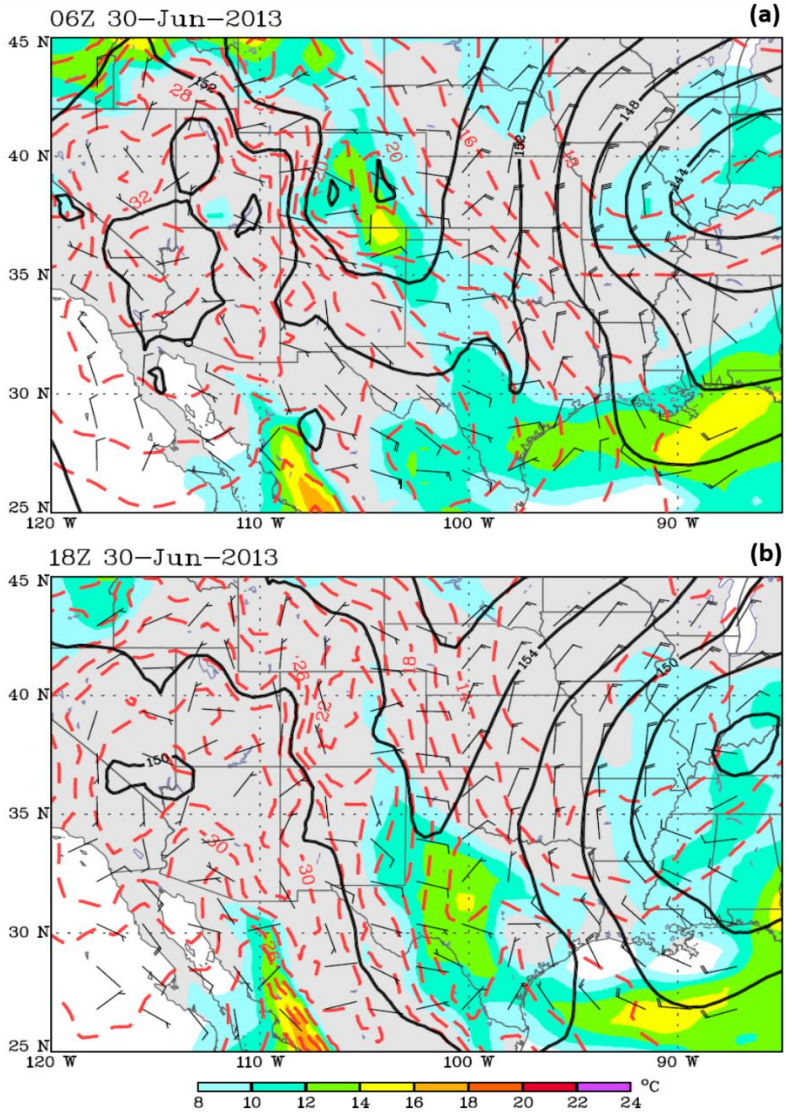

Figure 6. ERA-Interim [25] 850-hPa height (solid in m), temperature (red dashed in °C), wind barbs in kt, and dewpoint (fill in °C) valid at (**a**) 0600 UTC 30 June and (**b**) 1800 UTC 30 June 2013. These data analyses are original to this publication.

Deep tropospheric penetration of the unseasonably cool air into the IW occurred in association with these short-wave troughs. Cool air at both 700 hPa and 850 hPa penetrated over the Front Range into Western Colorado and Western New Mexico moving close to the CP as early as 06/30. The organization for this upstream cool air transport was the easterly and northeasterly flow accompanying the pressure rise zone depicted in Figure 7a,b along the Front Range of the Colorado and New Mexico Rocky Mountains in Figure 7a, subsequently, farther southwest into Northeastern Arizona in Figure 7b. Here, we see the 1008-hPa isoline in Figure 7a supplanted by the 1014-hPa isoline in Figure 7b over the northeastern half of Arizona during this 12-h period. These wind and mass adjustments, at least early on, are similar in structure to edge wave cold surges over the Western Great Plains adjacent to the Front Range of the Rocky Mountains [46]; however, they are advected unusually far west in this case. Shallow planetary boundary layer (PBL) damming of air against the Front Range occurred primarily during 03/30 and 15/30, as can be seen in Figure 6b at 850 hPa and, to a lesser extent, at 700 hPa in Figure 5b.

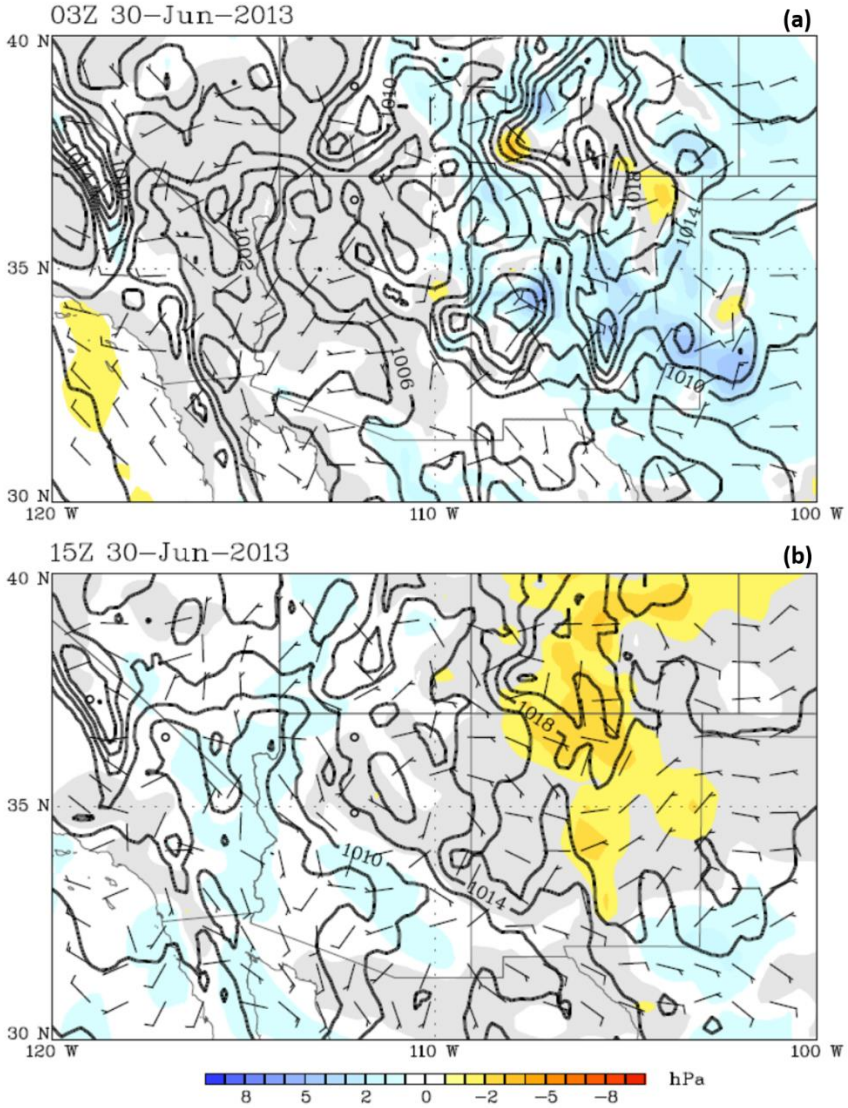

Figure 7. ERA5 [26] mean sea level pressure (solid in hPa), mean sea level 3-h pressure change (fill) in hPa, and surface wind barbs in kt valid at (**a**) 0300 UTC and (**b**) 1500 UTC 30 June 2013. These data analyses are original to this publication.

We define the unseasonably cool air in the PBL as being cool enough to cause the isoline of 850-hPa frontogenesis to be greater than 50 K 10^{-3} m^{-1} d^{-1}, as depicted in Figure 8a,b. In Figure 8a, the boundary at 06/30 is in West–Central Colorado and New Mexico, while, in Figure 8b, 12 h later, it is split into two zones: (1) in West–Central Colorado extending into North–Central and Southwestern New Mexico and (2) along the MR. These boundaries were established by the upstream (east–northeast origin) lower tropospheric penetration of polar air westward towards the Front Range followed by large-magnitude surface sensible heating over the CP. They were established first in proximity to 105° W at 06/30 accompanying cold air advection, then farther west 12 h later by 18/30 due to the surface heating of the CP, as indicated by the 700-hPa temperature increase in Figure 5b. The 700-hPa 318 decameter (dam) isoheight in Figure 5a,b was closely aligned with these fronts, indicating a boundary established by the combination of cold air advection and elevated terrain surface heating west of the Front Range. Note the effect of the differential heating and cooling across the frontogenesis regions on the isoheights accompanying the ridge over the Four Corners region. The differential heating has the effect of shifting the frontal geometry from a zonal orientation to a meridional orientation. This restructuring of the isoheights is consistent with the evolving mean sea level pressures, which increased in time

across this region, as can be seen in in Figure 7a,b, i.e., moving mass south–southwestwards across the High Plains of Colorado, New Mexico, and the Texas Panhandle towards and subsequently west of the Front Range.

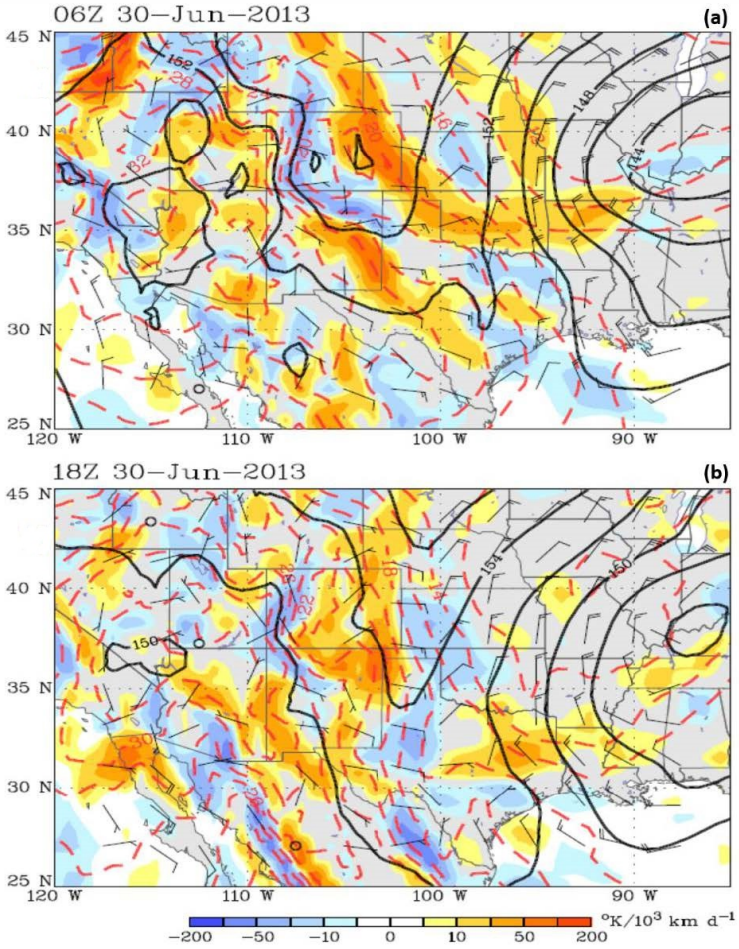

Figure 8. ERA-Interim [25] 850-hPa total frontogenesis (fill in K10^{-3} m^{-1} d^{-1}), height (solid in m), temperature (red dashed in °C), and wind barbs in kt valid at (**a**) 0600 UTC and (**b**) 1800 UTC 30 June 2013. These data analyses are original to this publication.

3.1.3. Moisture Transport in Response to Downscale Trough Organization and Frontogenesis

The previous adjustments in the mass and momentum fields were also accompanied by moisture transport predominantly westward into Eastern Arizona. More than 18 h prior to the YHFT, and during the early stages of the organization of the kinematics in the previous subsection, the modest, albeit important, moisture for Central Arizona convection was transported westwards into New Mexico and then Arizona. A shift to easterly flow at the surface over the plains and the Rocky Mountains accompanied the movements of pressure rises into the upper Rio Grande River Valley during the period spanning Figure 7a,b. Figures 9–12 reinforce this finding of the penetration of cool moist easterly wind up the Rio Grande and Pecos River Valleys of Texas and westward towards New Mexico in multiple pathways. This low-level moistening, particularly below 750 hPa, is evident in the 12/30 Santa Teresa (EPZ) and Albuquerque (ABQ) New Mexico soundings overnight during the early period of 30 June in Figure 9a,d. Figure 9b,d indicates that both low- and mid-level moisture increased in these soundings. The winds within the nocturnal PBL indicate a shallow easterly flow below an increasing northerly flow aloft. There are substantial dew point increases in both soundings (Figure 9b,d) overnight on 30 June.

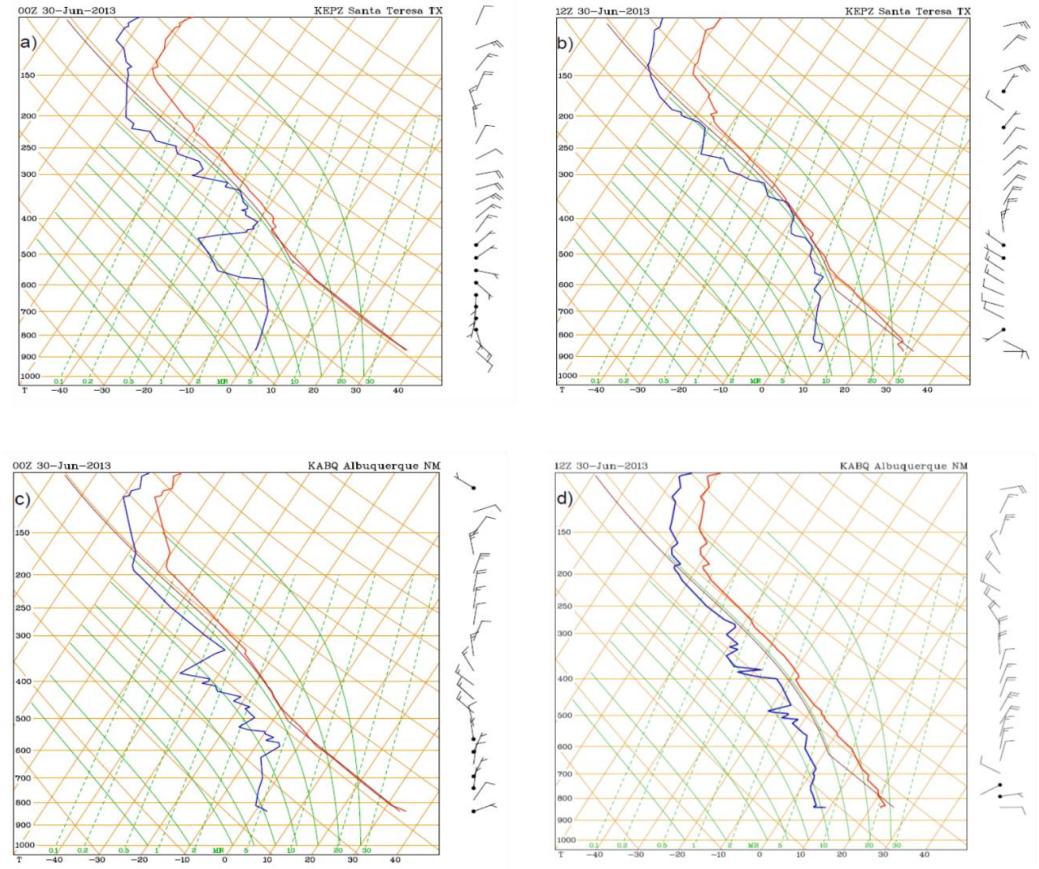

Figure 9. RAP (http://weather.rap.ucar.edu/upper/) Skew-T/log-P radiosonde soundings at (**a**,**b**) Santa Teresa, New Mexico (EPZ) and (**c**,**d**) Albuquerque, New Mexico (ABQ) valid at 0000 UTC and 1200 UTC 30 June 2013. These data analyses are original to this publication.

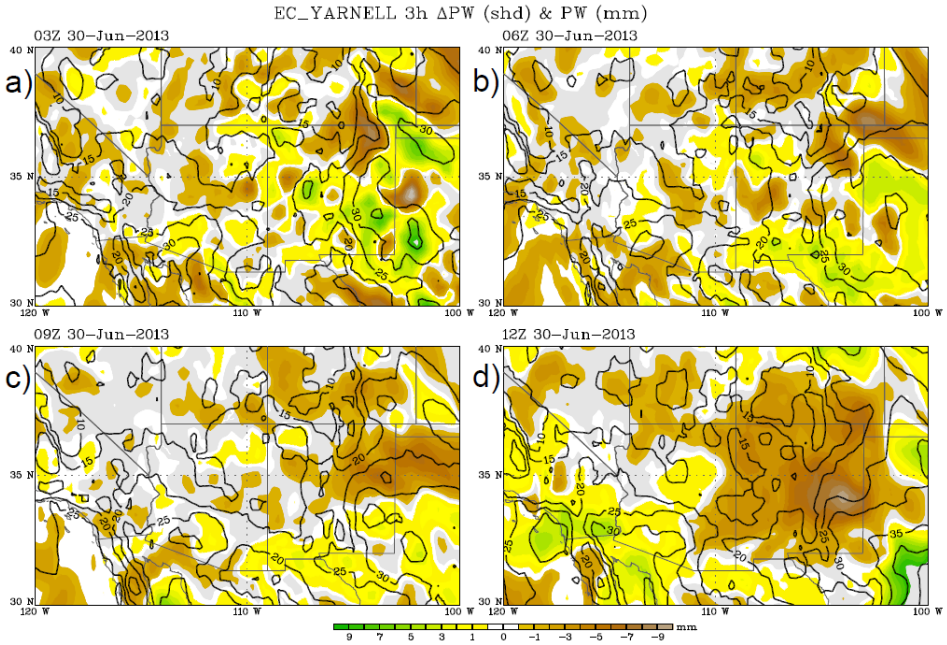

Figure 10. ERA-5 three-hour precipitable water change (in g kg^{-1} green and yellow fill (+) and brown fill (-)) and integrated precipitable water (black solid in g kg^{-1}) through the troposphere valid from (**a**) 0000–0300 UTC, (**b**) 0300–0600 UTC, (**c**) 0600–0900 UTC, and (**d**) 0900–1200 UTC 30 June 2013. These data analyses are original to this publication.

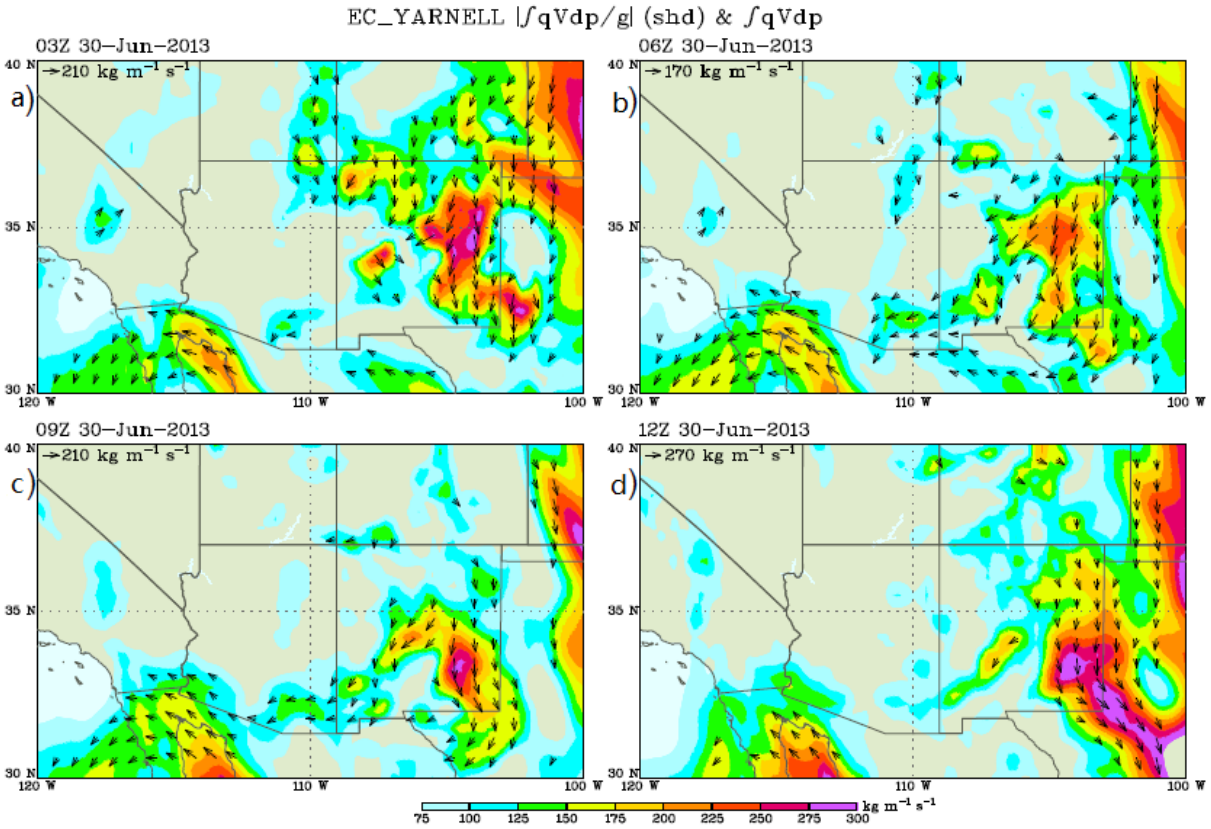

Figure 11. ERA5 [26] integrated moisture flux from the surface to 70 hPa (kg m^{-1} s^{-1}) and moisture flux vectors valid at (**a**) 0300 UTC, (**b**) 0600 UTC, (**c**) 0900 UTC, and (**d**) 1200 UTC 30 June 2013. These data analyses are original to this publication.

Precipitable water tendencies support this as well at 03/30, 06/30, 09/30, and 12/30 as a wave of increasing precipitable water values first arrived in East–Central New Mexico and then spread into Eastern Arizona, as depicted in Figure 10a–d. Additionally, in Figure 11a–d, the moisture flux vectors highlight how the moisture is transported westwards out of the High Plains and splits over the Rio Grande River Valley. One lobe moved across the San Juan River Valley into Northeastern Arizona and a second lobe across the Gila River Valley into Southeastern Arizona. The Chinle Wash and Little Colorado River Valley in the Navajo Nation, northeast of the MR and west of the Chuska and Carrizo Mountains seems to be a weak conduit of moisture towards the south–southwest in between the San Juan and Gila River Valleys. Little moisture arrived in the region from the Gulf of California, as the main flux was primarily towards Northeastern Arizona from the east. In Figure 12a–d, note the generally steady 10–15 °F dew point increases in the surface meteograms, primarily from 00/30 to 06/30, at Gallup (KGUP) and Deming (KDMN), New Mexico and somewhat later at Farmington, New Mexico (KFMN) and Prescott (KPRC), Arizona. Thus, the whole sequence of upstream RWBs, trough thinning, pressure rises, cold air advection, and subsequent frontogenesis described above allowed moisture to stream westward, displacing a very dry airmass over Arizona and preconditioning the region for convective development.

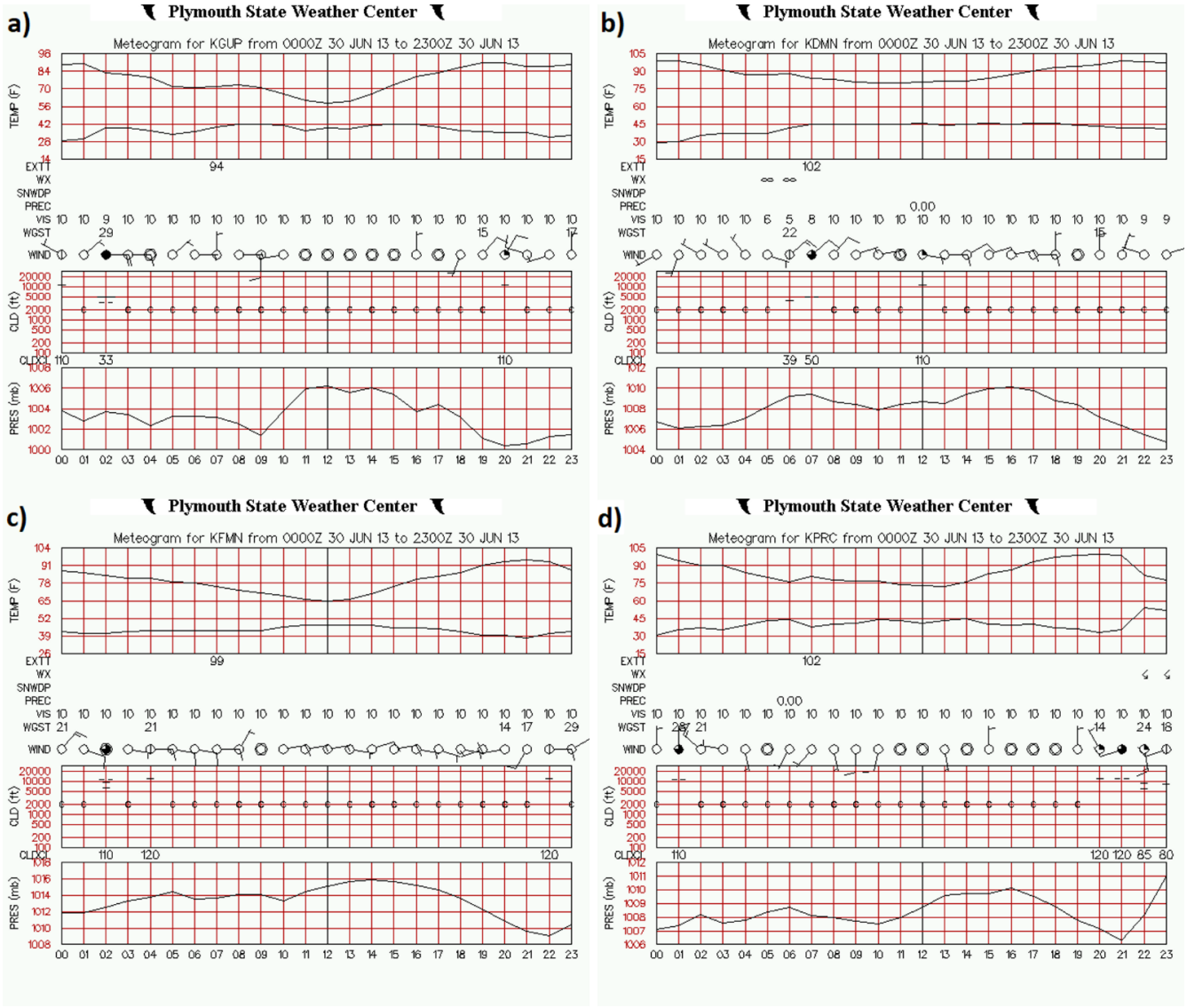

Figure 12. Surface meteograms [24] at (**a**) Gallup, New Mexico (KGUP), (**b**) Deming, New Mexico (KDMN), (**c**) Farmington, New Mexico (KFMN), and (**d**) Prescott, Arizona (KPRC) reprenting the entire period from 0000 UTC to 2300 UTC 30 June 2013. These data analyses are original to this publication.

3.2. Regional Circulations Organizing Convection at the Meso-β Scale

In this section, we use WRF-ARW 2.3-km and 0.777-km simulations to explore the organization of the environment for the triggering and subsequent propagation of convection.

3.2.1. Dual Jetlet (J1 and J2) Evolution and Divergent Circulation Organizing Convection

As early as 12/30, the flow over the IW exhibited subsynoptic jets analogous to mesoscale jetlets [47–49]. These features were shifted westwards from the polar jet located over Eastern Kansas (Figure 4e). The jets modify the upper-level divergence and vertical shear that control the triggering and structure of convection. The WRF-ARW 2.3-km simulated wind vectors resolve a weak secondary flow maximum in the 200–300-hPa layer from the west–northwest at the meso-α scale located over the region extending from Southwestern Utah through Southeastern New Mexico (note elongated wind and potential vorticity maxima in Figure 13a,c,e). This feature, the primary jetlet (J1), encompassed an area of approximately 1300 km in length and 200 km in width and was centered near the Southwestern Colorado–Northwestern New Mexico border at 12/30. J1 represents a

subsynoptic west–northwesterly airflow with a maximum core approximately 15–20 m s^{-1} surrounded by a broader scale region of winds > 10 m s^{-1}. This is located far (>1500 km) upstream from the polar jet core and main baroclinic zone in Eastern Kansas. The J1 core propagated through Northwestern New Mexico just east of the Arizona border during the 14/30–18/30 period (Figure 13b,d,f). J1 was closely aligned with the 700–850-hPa thermal boundary in Figure 8a that is just east of the Four Corners region.

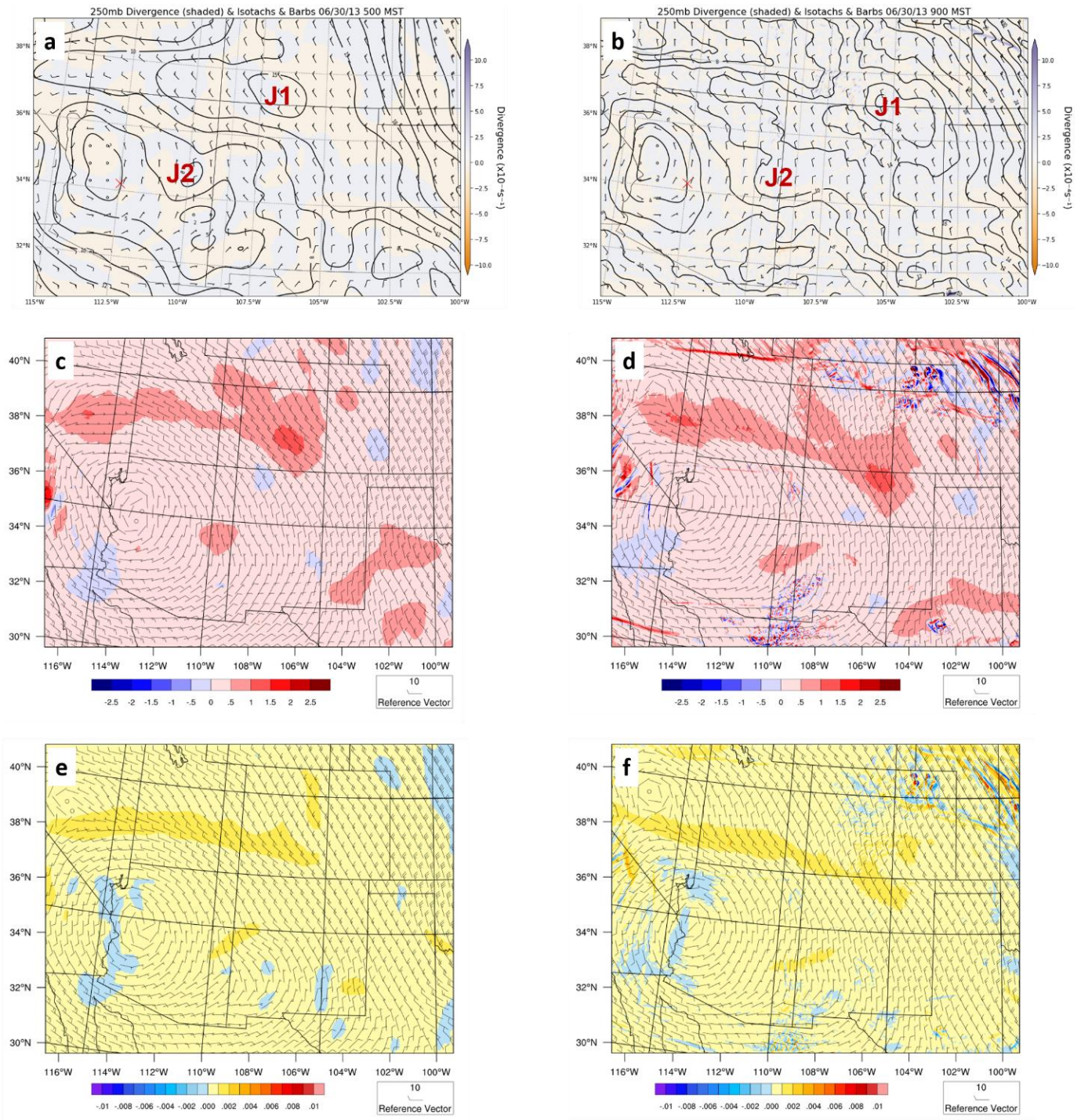

Figure 13. WRF-ARW-simulated 2.3-km meso-α scale (**a**,**b**) 250-hPa divergence (fill in 10^{-4} s^{-1}) isotachs (fill in m s^{-1}) and wind barbs (m s^{-1}), (**c**,**d**) 250-hPa potential vorticity (fill in 10^{-6} s^{-1} PVU) and wind barbs (m s^{-1}), and (**e**,**f**) 250-hPa inertial instability parameter (fill in s^{-2}) and wind barbs (ms^{-1}) all valid at (**a**,**c**,**e**) 1200 UTC and (**b**,**d**,**f**) 1600 UTC 30 June 2013. X is the Bradshaw Mountains.

Commencing just before 12/30 and thereafter, the right entrance region of J1 split off into another a smaller (meso-β scale) jetlet, the secondary jetlet (J2), that propagated into Northeastern Arizona: (1) between the MR and the Chuska and the Carrizo Mountains and (2) southwest of Canyon de Chelly and the Defiance Plateau. J2 organized into an anticyclonically curved wind maximum (Figure 13a,b). J2 within the J1 right entrance region enhanced the upper-level divergence as the surface sensible heating proceeded above the MR and southwestward through the Weaver Mountains on 30 June. It was shown that J2 was associated with an enhanced vertical wind shear that could support the multicellular convective density currents [23].

The calculations were performed in this section to establish the fundamental dynamical characteristics of J1 and J2 during 12/30–18/30. J1 achieved a scale of approximately the Rossby radius of deformation (L_r) in the region between Southwestern Utah and Southeastern New Mexico. Thus, J1 could be considered to become a coherent or autonomous jet at the meso-α scale with an along-stream length of approximately L_r. J2, in contrast, represents an adjustment within the right entrance region of J1 and is a jetlet that likely deviates from the thermal wind balance at a scale much less than L_r. J1 is more closely approaching a semi-geostrophic jet streak circulation in scale, and J2 is highly ageostrophic and non-gradient during J1's developmental process. J2's ageostrophic vector is directed opposite to the balanced semi-geostrophic thermal wind flow, i.e., streamwise and towards the right in the entrance region as it strengthens in response to the inertial–advective forcing directed towards the south–southeast. This inertial–advective acceleration in J2 opposes the cross-frontal pressure gradient force directed to the northeast within J1's entrance region.

The L_r can be defined by the following equation:

$$L_r = \frac{NH}{2\pi f} \tag{1}$$

where (1) N is the Brunt-Vaisala frequency, (2) H is the scale height of the circulation, and (3) f is the Coriolis parameter [50]. If one assumes the following: (1) H is approximately 10 km, as the feature extends to approximately 200 hPa or approximately 12,000 m MSL, which is approximately 10,000 m above the average terrain height of approximately 2000 m in northeastern Arizona, (2) f is approximately 8.35×10^{-5} s^{-1} at 35° N latitude, and (3) N is defined:

$$N = \sqrt{\frac{g}{\theta}\frac{\Delta\theta}{\Delta z}} \tag{2}$$

Then, for an average column (H) between 800 and 200 hPa, an average potential temperature of 322 K, and an average lapse rate over the depth of H, including the PBL, mid-troposphere, and upper-troposphere of approximately 4 K (2500 m^{-1}), N is approximately 0.007 s^{-1}, and L_r is approximately 1350 km. Additionally, if the inertial period is defined:

$$\tau = \frac{2\pi}{f} \tag{3}$$

which is approximately 21 h at this latitude, then J1 exceeds that period and equals that length scale by lasting at least 24 h, as well as approximating the L_r, respectively. Conversely, J2 does not come close to this L_r or τ, as it lasts only approximately 6–8 h over approximately 400–600 km. It is plausible, therefore, that J1 is approaching a balance in a semi-geostrophic sense, but J2 is not. Therefore, the extent of J2 is substantially less than the L_r in both x- and y-space, as is its period (Figure 13c,d). Additionally, the representative geostrophic wind and anticyclonic gradient wind in the J1 right entrance region over Southern Utah and Northern Arizona are calculated employing the following equations from Lin [50]:

$$V_{geo} = \frac{1}{f}\frac{\Delta\Phi}{\Delta D} \tag{4}$$

$$V_{grad} = rf - \sqrt{r^2 f^2 - 4rfV_{geo}/2} \quad (5)$$

We will assume, based on close analyses of the 2.3-km simulated fields, that: (1) $\Delta\Phi$ represents a geopotential height difference of approximately 50 geopotential meters (gpm) over ΔD, which is a southwest–northeast orthogonal transect length through the right entrance region of J1, (2) the right entrance region is assumed to be approximately 200 km in size at 250 hPa over Northeastern Arizona, and (3) r is the radius of curvature of approximately 300 km based on the wind structure from the center of the ridge to J2 in the same region, as can be inferred from Figure 15a at 14/30. The calculations in Equations (4) and (5) indicate a representative northwesterly geostrophic wind within the J1 entrance region of approximately 5 m s^{-1}, where the total wind velocity is approximately 10 m s^{-1} at 250 hPa, with a gradient wind of approximately 7.5 m s^{-1}. These are consistent with an unbalanced (in the thermal wind sense), supergeostrophic, and rightward-directed flow out of the J1 entrance region, as can be seen in Figure 13a and Figure 15a in the region between 111° W and 112° W and between 34 and 36° N at 14/30. The flow is also a supergradient in the right entrance region of J1, indicating low inertial stability as the potential vorticity approaches 0 PVU (Figure 13c,d), and the inertial stability parameter defined as:

$$f\left(\frac{DV_{geo}}{Dx} + f\right) \quad (6)$$

is near 0, indicating inertial neutrality transitioning to instability (Figure 13e,f) [50]. The low inertial stability above the region northeast of the MR existed near the subsynoptic front over the eastern part of the CP in the 700–850-hPa layer in Figures 5, 6 and 8. These calculations support a circulation that evolves into J2 that is not in a quasi-geostrophic, semi-geostrophic, or gradient wind balance. In short, J2 is one where both the Eulerian and the Lagrangian Rossby numbers at 250–300 hPa defined as:

$$RoE = \frac{(V \cdot \nabla V)}{fV} \quad (7)$$

$$RoL = \frac{1}{fV}\frac{DV}{Dt} \quad (8)$$

approach 1.25 and 1.15, respectively, exceeding the criterion for imbalance [51] in the right entrance region of the jetlet. These calculations assume: (1) approximately 7.5 m s^{-1} total wind velocity, (2) approximately 5 m s^{-1} total velocity gradient over 50 km, (3) approximately 2.5 m s^{-1} average Lagrangian acceleration over the 3600 s periods between 1300 UTC 30 June and 1600 UTC 30 June, 2013 encompassing the region in between 110.5° and 111.5° W and between 34.25° and 35.5° N, i.e., above the MR and Black Hills during this period, and (4) f is approximately 8.35×10^{-5} s^{-1} at 35° N. RoE and RoL are both >1.00 consistent with an unbalanced flow deviating from thermal wind balance. Figure 14c,d depicts the development of a 250-hPa–700-hPa differential divergence, which is generally juxtaposed with rightward- and equatorward-directed ageostrophic flows within J2 emerging from J1′s entrance region. This ageostrophy reflects the splitting plume of the momentum away from J1 into J2. This momentum advection is evidenced by a strengthening of the wind observed in J2′s right exit region between 111.5° and 112.5° W and between 34.25° to 35° N northeast and east of Yarnell during the 14/30–18/30 period above the MR and Black Hills (Figure 15a,c).

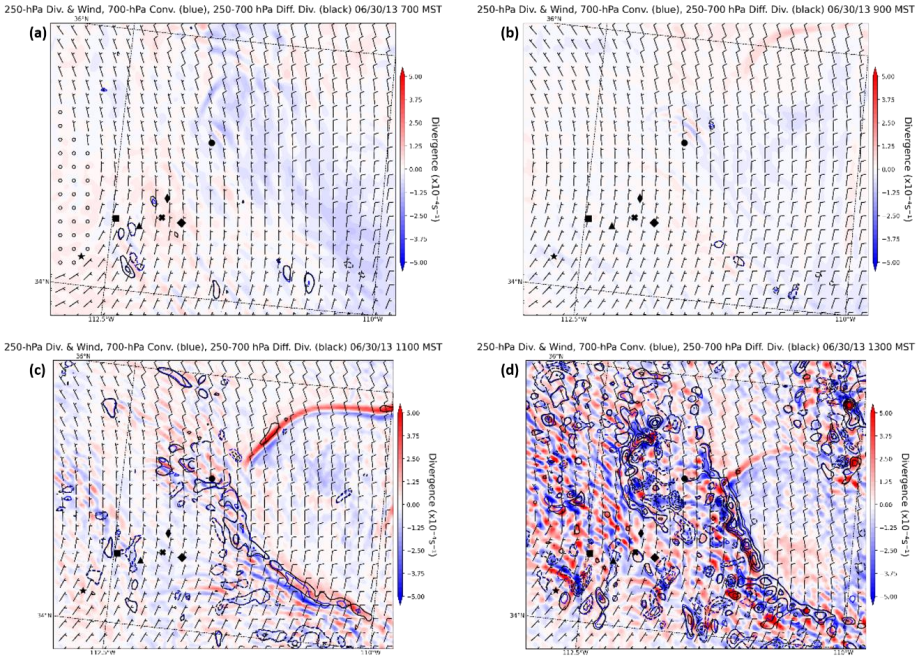

Figure 14. WRF-ARW-simulated 2.3-km meso-β-scale 700-hPa convergence (blue solid in $10^{-6}s^{-1}$), 250–700 differential divergence (black solid in $10^{-6}s^{-1}$), and 250-hPa divergence (fill in $10^{-6}s^{-1}$) valid at (**a**) 1400 UTC, (**b**) 1600 UTC, (**c**) 1800 UTC, and (**d**) 2000 UTC 30 June 2013. Icons are place locators as in Figure 3a.

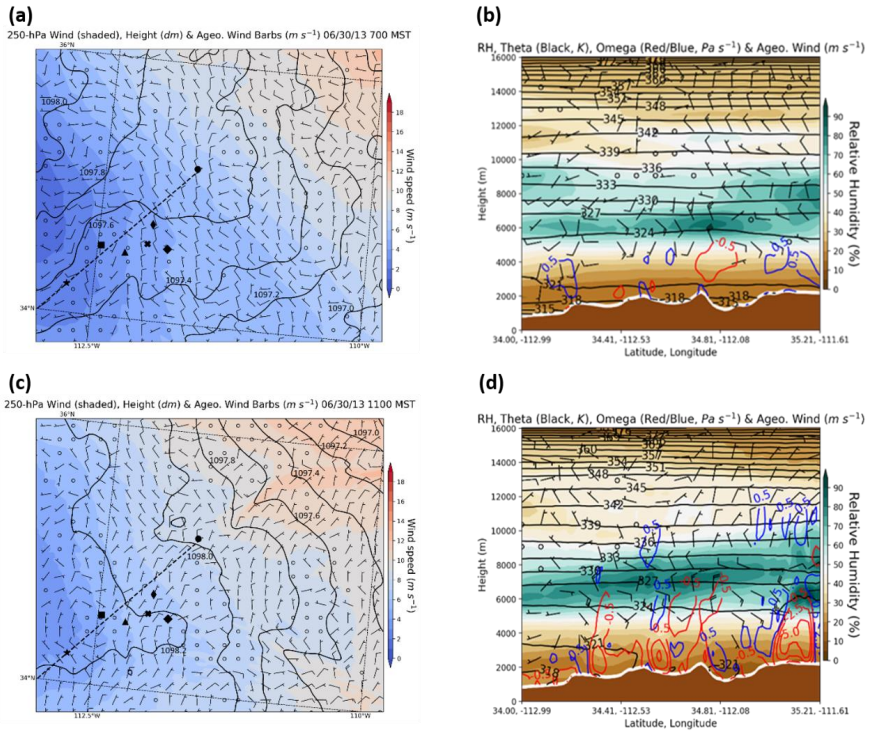

Figure 15. WRF-ARW-simulated 2.3-km meso-β-scale 250-hPa ageostrophic wind barbs (m s^{-1}), height (solid in dam), total wind isotachs (fill in kt) valid at (**a**) 1400 UTC and (**c**) 1800 UTC and ageostrophic vectors (kt), potential temperature (blue solid in K and in vertical spacing increasing with height), omega (red- and blue+ = solid in μb s^{-1}), and relative humidity (fill in %) from 34° N, 112.99° W to 35.2° N, 111.6° W valid at (**b**) 1400 UTC and (**d**) 1800 TC 30 June 2013. Icons are place locators as in Figure 3a. Vertical cross-section location from 34° N, 112.99° W to 35.2° N, 111.6° W in (**b**,**d**) depicted on (**a**,**c**) with a black dashed line.

Vertically differential divergence develops above the MR in the right exit region of J2. This ageostrophy, consistent with these calculations in this section, can be seen in Figure 15a,c, as well as vertical cross-sections in Figure 15b,d. The locations for ageostrophic vectors directed first to the south–southeast and, subsequently, to the southwest, respectively, primarily surround the black dot representing the location of KFLG in Figure 15a,c. These features above 6000 m MSL in Figure 15b,d can be seen to the northeast of Flagstaff over the MR (right side of the cross-section extending downstream from the location at 34.81° N and 112.08° W).

Additionally seen in Figure 15b,d is the early mid-tropospheric ascent over the MR, Verde Valley, and Black Hills, followed by late-morning lower tropospheric ascent due to Mountain Plains Solenoidal (MPS) forcing [52,53]. This ascent intensifies primarily on the northeastern side of all the mountains between the MR and Weaver Mountains. This indicates the transition from the divergence aloft with J2 to MPS differential heating between the mountains and plains during the morning hours. Note how the cross-sections in Figure 15b,d depict the shift in ageostrophic airflow from (1) the north–northwest to south–southeast to (2) east–northeast to south–southwest aloft as the low-level thermally direct circulation comes into the phase with the exit region of J2. This reflects, at 600 hPa, the broader-scale and lower-level height/thickness rises due to diurnal sensible heating immediately above the elevated plateau, which gives way to a region of moist convective heating-induced height falls as the level of moist convective heating becomes more elevated relative to MPS heating, the net effect being to reorient the acceleration vector aloft towards the southwest, as is shown in Figures 15 and 16.

3.2.2. Signal of Enhanced/Spatially Variable Convective Instability, Downdraft Potential, and Vertical Wind Shear

The downscale circulations resulted in organized patterns of ascending motions and changes in static stability, as well as vertical wind shear that control the triggering and evolution of convective density currents. Figure 16 demonstrates the organization of the simulated squall line over the MR and its intensifying northwesterly low-level flow. Figures 17 and 18, respectively, depict the WRF 2.3-km-simulated evolution of (1) MUCAPE and (2) soundings from which we calculate the Downdraft Convective Available Potential Energy (DCAPE) from northeast to southwest across the MR and Yavapai County between 16/30 and 22/30 UTC. This is during the period when the mesoscale ascent accompanying J2 gives way to the growing MPS circulation and its interaction with J2 above the MR. These processes signal a rapidly increasing zone of both convective instability and strong downdraft potential over the MR and most of Yavapai County in Central Arizona.

As can be seen in Figures 17 and 18, the initial MUCAPE maxima at 1700 UTC are separated from the MR, as they are in Southwestern and Eastern Arizona representing, respectively, the hotter low-level PBL air and richer plume of integrated moisture flux, as depicted in Figures 8b and 11h. The early significant Surface-Based Convective Inhibition (SBCIN) in Southwestern Arizona rendered this large magnitude zone of MUCAPE irrelevant to the organization of convection. This changed later in the period as the ascent under J2 propagated towards the southwest and surface heating increased. In time, the ascending flow over and just southwest of the MR, in conjunction with the intensifying surface heating accompanying the multiple MPS above the Black Hills, Bradshaw Mountains, and Weaver Mountains, created a juxtaposed region of increasing MUCAPE over and southwest of the MR, as well as increasing the DCAPE in Central Arizona. The southwest–northeast gradients of MUCAPE and DCAPE and northeast–southwest gradients of lower mid-tropospheric vertical wind shears can be inferred from Figures 17 and 18. The southwest–northeast gradient of MUCAPE increases temporally in Figure 17. In Figure 18, the northeast–southwest gradient of the vertical wind shear increases, as the descending layer of the northeast flow was greater to the northeast under a slightly stronger north–northeasterly flow with J2. The northerly wind component extends down to 700 hPa in the Black Hills in Figure 18b, with a nearly southerly flow at the surface, but weakens to the southwest, e.g., the northerly wind component is above 650 hPa in the Weaver

Mountains in Figure 18d, with nearly uniform westerly flow at the surface. During 18/30–22/30, the MUCAPE in Figure 17 increased and filled in the region between the Black Hills and Yarnell with the largest values increasing towards the southwest. Additionally, the specific simulated soundings in Figure 18a–d, moving from the MR to the Black Hills, Bradshaw Mountains, and Weaver Mountains, respectively, showed a progression during the period from 1800 UTC 30 June to 2300 UTC 30 June, 2013 of more DCAPE (1165, 1561, 1690, and 1924 J kg^{-1}, respectively) and reduced the directional wind shears in the vertical in the lower mid-troposphere (700–850-hPa layer) as one progressed southwestwards, indicating a transition from an environment favorable for linear density current or squall line structures towards an environment conducive to microbursts. This was exemplified by an increased vertical wind shear to the northeast and increased downdraft potential to the southwest, with a 1924-J kg^{-1} value representing an exceptional downdraft potential.

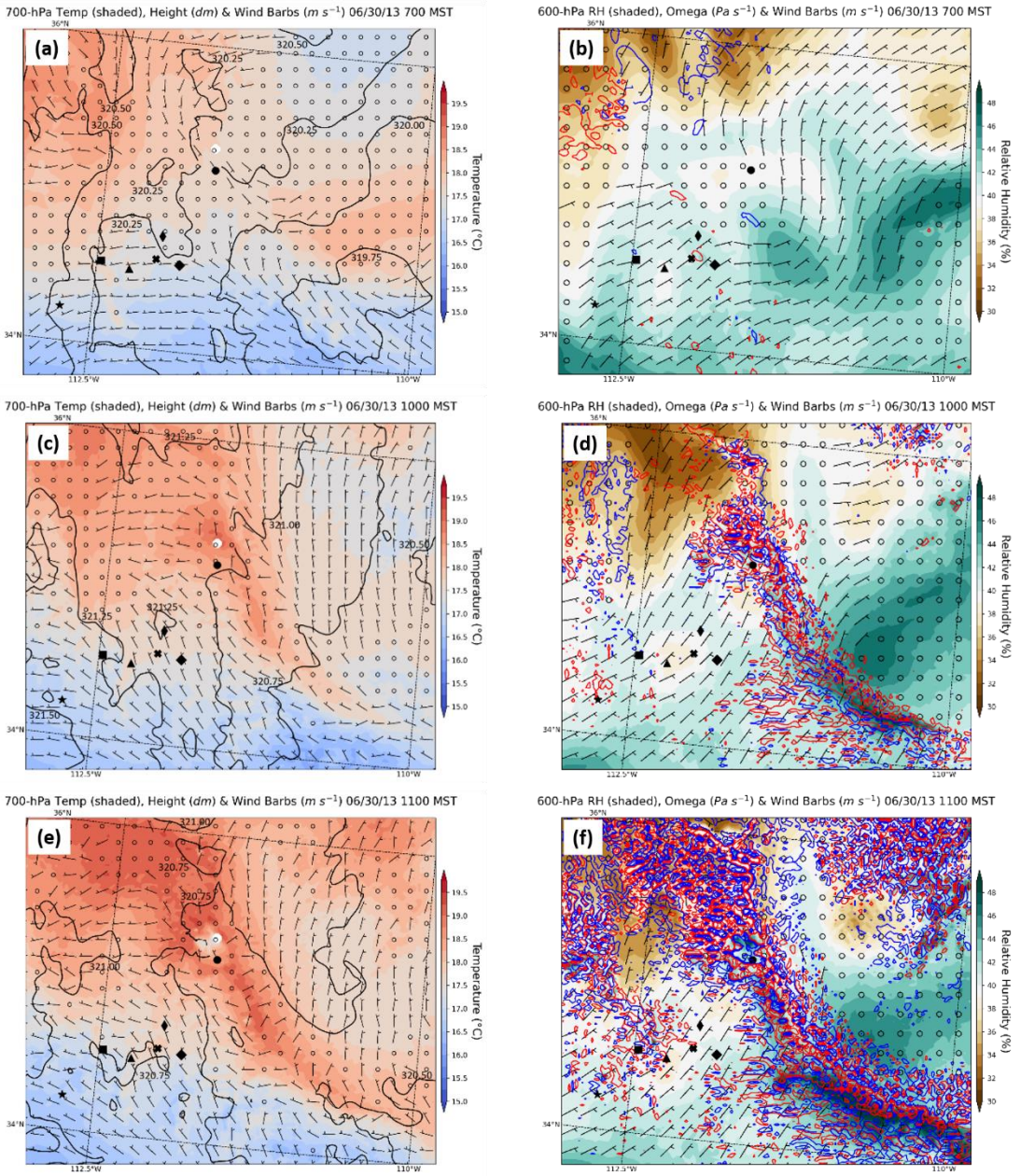

Figure 16. WRF-ARW-simulated 2.3-km meso-β-scale 700-hPa temperatures (red dashed in °C), isoheights (solid in dam), and wind barbs (m s^{-1}) and 600-hPa omega (red- and blue+ = solid in μb s^{-1}), wind barbs (m s^{-1}), and 600-hPa relative humidity (fill in %) valid at (**a**,**b**) 1400 UTC, (**c**,**d**) 1700 UTC, and (**e**,**f**) 1800 UTC 30 June 2013. Icons are place locators as in Figure 3a.

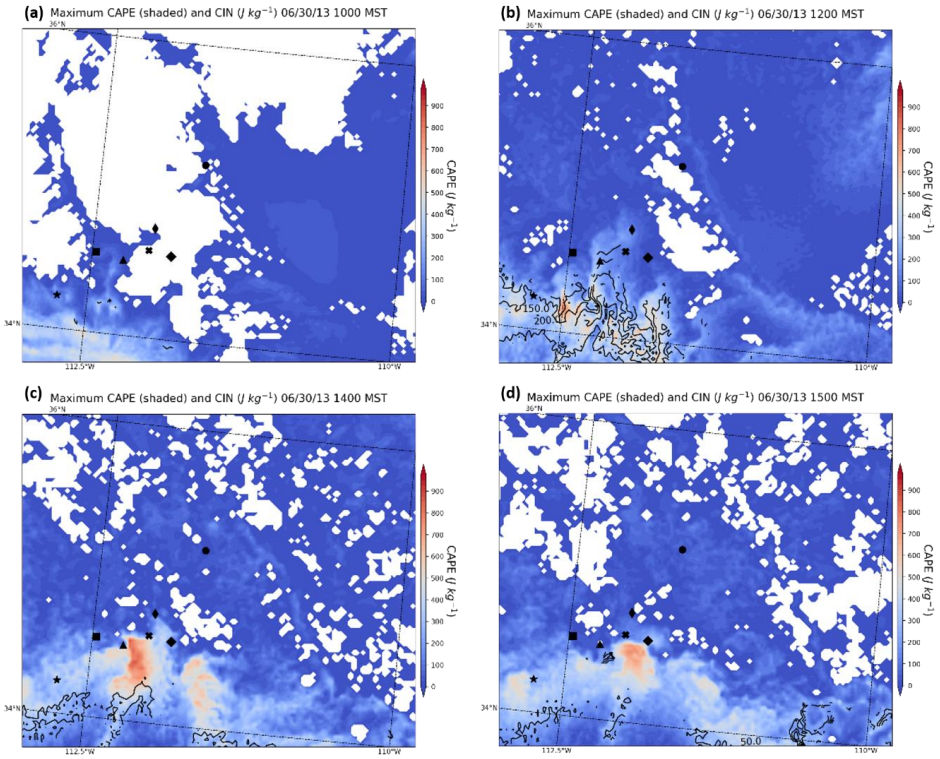

Figure 17. WRF-ARW-simulated 2.3-km meso-β-scale MUCAPE (fill in j kg^{-1}) and CIN (black solid in J kg^{-1}) valid at (**a**) 1700 UTC, (**b**) 1900 UTC, (**c**) 2100 UTC, and (**d**) 2200 UTC 30 June 2013. Icons are place locators as in Figure 3a.

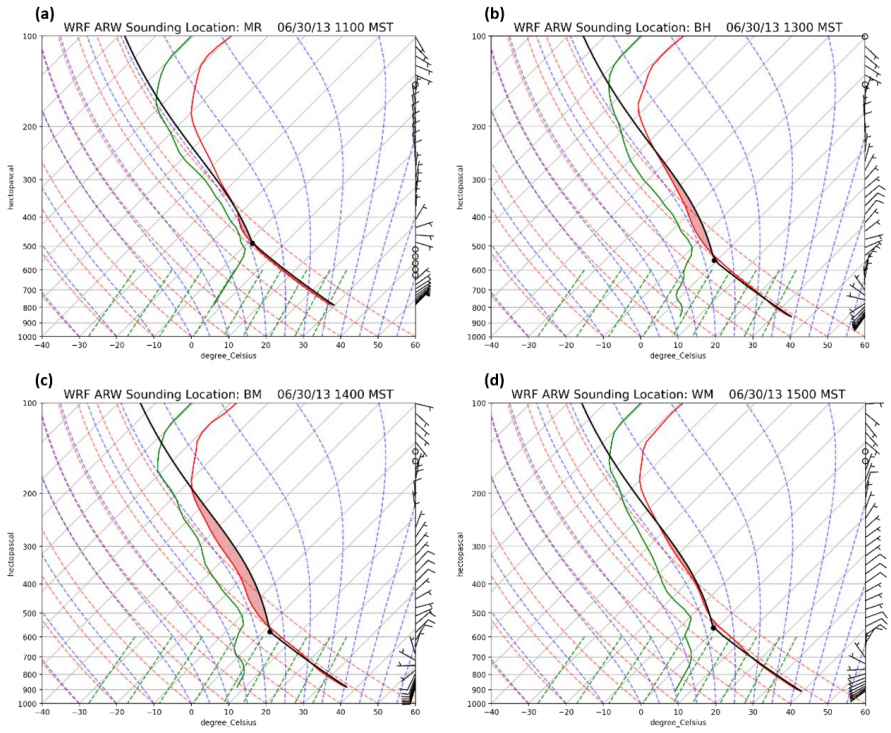

Figure 18. WRF-ARW-simulated 2.3-km meso-β-scale soundings located at (**a**) the Mogollon Rim at 1800 UTC (35.24° N, 111.72° W, CAPE = 56 J/Kg, DCAPE = 1165 J Kg^{-1}), (**b**) Black Hills at 2000 UTC (34.61° N, 112.19° W, CAPE = 365 J Kg^{-1}, DCAPE = 1561 J Kg^{-1}), (**c**) Bradshaw Mountains at 2100 UTC (34.54° N, 112.32° W, CAPE = 816 J Kg^{-1}, DCAPE = 1690 J Kg^{-1}), and (**d**) Weaver Mountains at 2300 UTC (34.26° N, 112.84° W, CAPE = 66 J Kg^{-1}, DCAPE = 1924 J Kg^{-1}) 30 June 2013.

3.3. Observed Radar and Simulated Meso-β/γ Scale Low-Level Winds

3.3.1. Observed Radar Evolution

The evolving radar imagery indicates the organized nature of the convection that propagated from the MR to Yarnell. The first organized convective cells on 30 June developed at ~1815 UTC in two fundamental clusters that evolved into lines: (1) over the immediate region near KFLG just after 1815 UTC, which is the best-developed line (L2), and (2) between Kingman, AZ (KIGM), and Seligman, AZ just before 1815 UTC, which is the first line (L1) (Figure 19a). By 1915 UTC, new cells developed in these two lines along and just northwest of the MR and southeast of KFLG (Figure 19b), with the strongest cells northwest of KFLG in L2 and southeast of KIGM in L1. These locations are close to the early divergence and ascent under J2 in Figures 13–16. During this hour, better organization of the cells southeast of KFLG created a new line along the MR (Figure 19b). This line is under the divergent J2 flow, as depicted in Figures 13–16, but is short lived.

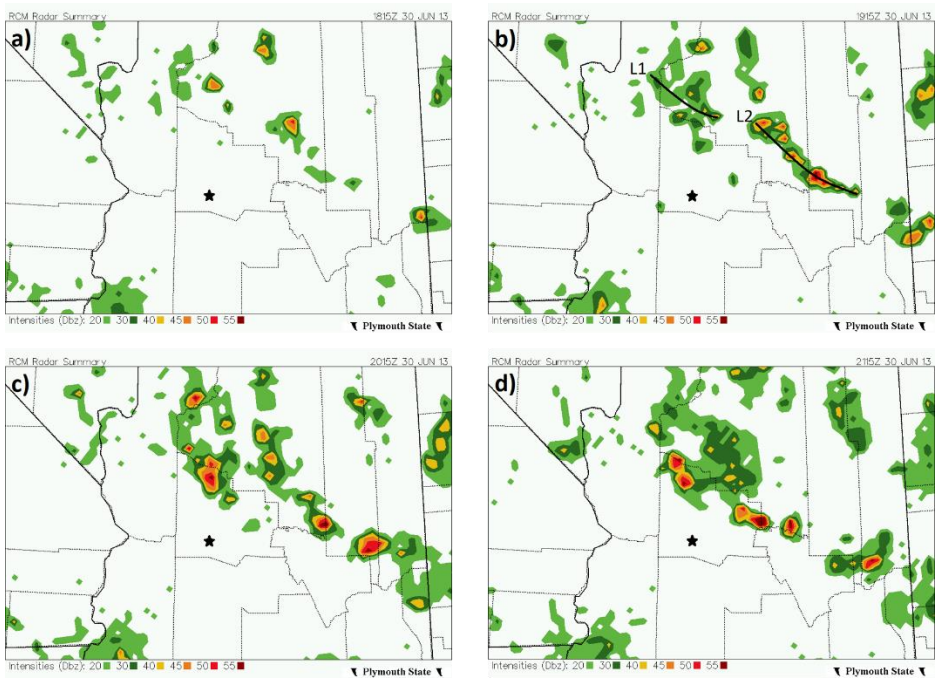

Figure 19. Radar Coded Message (RCM) radar summary for Central and Northern Arizona valid at (**a**) 1815 UTC, (**b**) 1915 UTC, (**c**) 2015 UTC, and (**d**) 2115 UTC 30 June 2013 [24] Yarnell, Arizona depicted with a black star, and L1 and L2 are propagating convective lines. These data analyses are original to this publication.

Following these initial, somewhat transitory signals of convection, a second wave of convection develops, stronger and better organized than the first stage, just southwest of the MR over the Black Hills. The radar reflectivity mosaics in Figure 19c,d suggest that this second stage of convection was coupled to low-level outflow from the initial L2 convection near KFLG. At 2115 and 2132 UTC, in Figures 19d and 20a,b, the reflectivity mosaics and comparisons between Doppler radars at KFSX and Phoenix Sky Harbor International Airport (TPHX) strongly suggest that there was: (1) a surface outflow boundary that was bow-shaped extending southeastward against the low-level southwesterly flow from the northeast corner of Yavapai County to Southeastern Yavapai County and (2) a well-organized cell or cell cluster in Northwestern Yavapai County. At approximately 2115 UTC, an isolated but strong cell developed with L2 over the Black Hills in Northeastern Yavapai County between Cherry and Dewey-Humboldt. This strong cell quickly approached 50 dBZ and then became flanked by many more cells, both to the northwest and southeast, over the next 30–60 min, forming a vigorous bowing line propagating against the low-level

southwesterly flow, derivative of the L2 in Figure 19a,b, as it moved through the Prescott, AZ (KPRC) area.

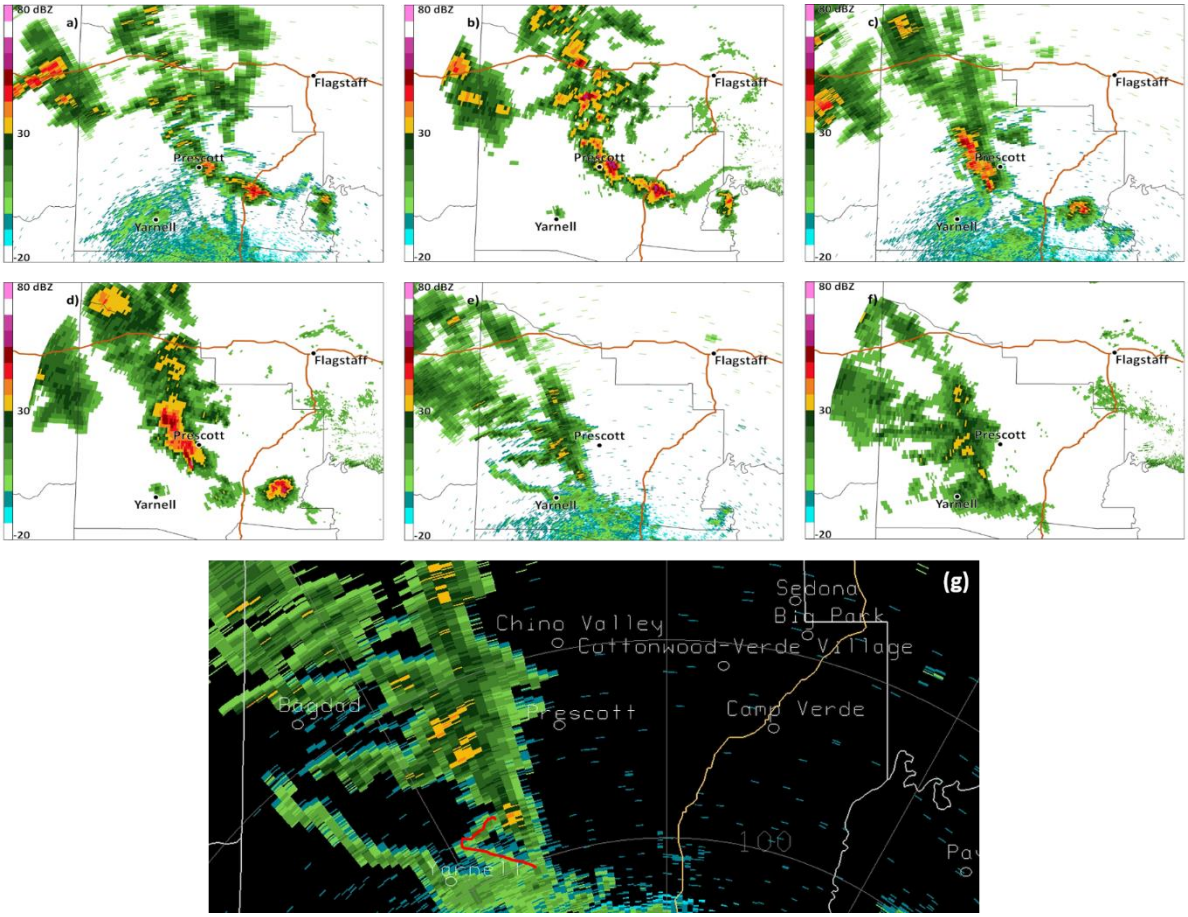

Figure 20. Alternating TPHX and KFSX radar imagery [27] zoomed into Yavapai County, Arizona valid at (**a**,**b**) 2132 UTC, (**c**,**d**) 2228 UTC, (**e**,**f**) 2330 UTC 30 June 2013 (NOAA-NIDS 2020: TPHX Doppler), and (**g**) zoomed in view of (f), with the red line indicating a microburst outflow. Prescott and Flagstaff, Arizona are depicted with black dots. These data analyses are original to this publication.

During the period between 2100 UTC 30 June and 2300 UTC 30 June 2013 in Figure 20c–f, the developing cell on the northeast side of the Black Hills was flanked by very substantial cells $\geq$ 50 dBZ on the northwest side of the Black Hills approaching the Bradshaw Mountains. Two fundamental areas of convective evolution were evident: (1) the L1 became consolidated northwest of the Black Hills and was approaching the Bradshaw Mountains in West–Central Yavapai County and (2) the L2 outflow arrived between the Black Hills and Bradshaw Mountains as a bow-shaped line, which moved towards the region just northeast of Yarnell in Central Yavapai County. The KPRC meteogram in Figure 12d supports the occurrence of cool air outflow/mean sea level pressure rises which occurred from 2100 UTC 30 June to 2200 UTC 30 June, 2013 with L2. These two groups of convection, accompanying the L1 and L2 features, represented the most outstanding convective organization in the region and existed at the same time as the mid-upper-tropospheric ascending circulations were aligned and peaked in intensity at ~22/30 when the MUCAPE spread into the region, including the Bradshaw Mountains, in Figure 17c,d. Hence, deep convective organization and high dBZ radar signals developed over the mountains in Yavapai County.

Finally, during the period just before and just after 23/30 in Figure 20e,f, the TPHX and KFSX reflectivity along the main northwest–southeast line of cells over the Bradshaw Mountains (eastern part of the L1) weakened to ~30 dBZ, while a new area of convec-

tion became oriented northeast–southwest on the southeastern flank of the Bradshaw Mountains/northwestern flank of the Eastern Weaver Mountains and extended southwestward to the Yarnell Hill plume evidenced by a weak ~20-dBZ echo in Figure 20b,d. In Figure 21a–d, dual-polarimetric radar data from KFSX indicate that, during the period between 2100 UTC 30 June and 0000 UTC 1 July 2013, 0.6 or lower correlation coefficient (CC) values were generally contained within the fire plume, indicating a large variety of particle types [54]. During this period, the position of the plume shifted from northeast (Figure 21a) to east (Figure 21b), then southeast (Figure 21c), and then south–southwest (Figure 21d) of the burn area. The position of the plume relative to the burn area indicates the tilt of the plume, with the height and a progression of wind directions from southwest to west to northwest to north northeast. Mostly positive differential reflectivity (ZDR) values ranging up to 8.0 dBZ were observed within the plume (not shown), indicating mainly horizontally aligned particles, likely including ash, in the vicinity of the strengthening plume and pyrocumulus clouds. These polarimetric signatures occur as a bow-shaped region of smaller more spherical particles with higher CC values, lower ZDR values, and reflectivity <30 dBZ and propagate towards Yarnell from the Bradshaw Mountains, corresponding to the advance of mid-level clouds ahead of the dissipating convective line. Precipitation from this line is mainly virga and light rain (as revealed by photographic evidence and radar observations).

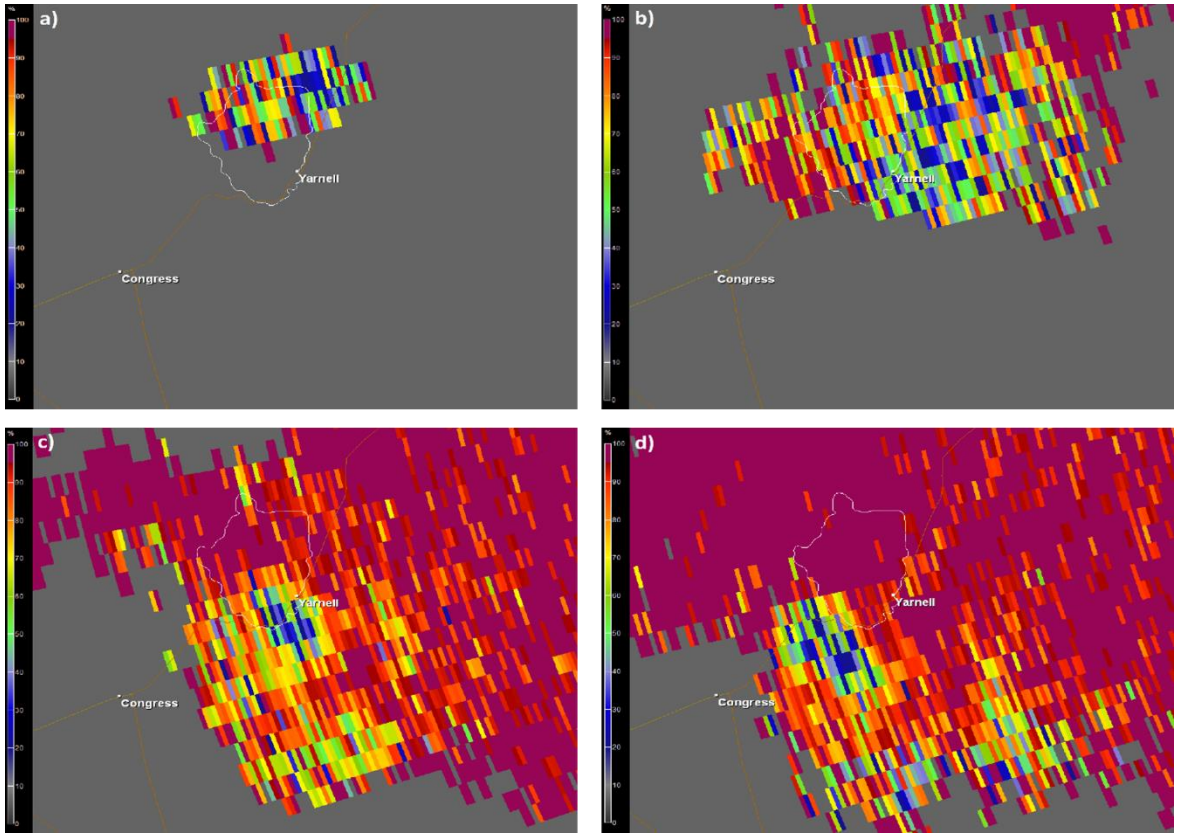

Figure 21. KFSX dual-polarimetric correlation coefficient [27] from the 0.5° base elevation scan zoomed into the region surrounding Yarnell, Arizona valid at (**a**) 2117 UTC, (**b**) 2305 UTC, (**c**) 2334 UTC, and (**d**) 2352 UTC 30 June 2013**.** The thin white contour denotes the Yarnell Hill burn area. These data analyses are original to this publication.

3.3.2. Simulated Meso-β/γ-Scale Low-Level Winds

Figure 22a–g indicates the longevity and intensity of the convectively driven surface density current and its southwestward propagation against the surface flow from the MR to Yarnell. These figures from the WRF 777-m simulation are located along the vertical

cross-section depicted in Figure 3a, while the WRF 777-m-simulated Figure 22h is centered near Yarnell [13].

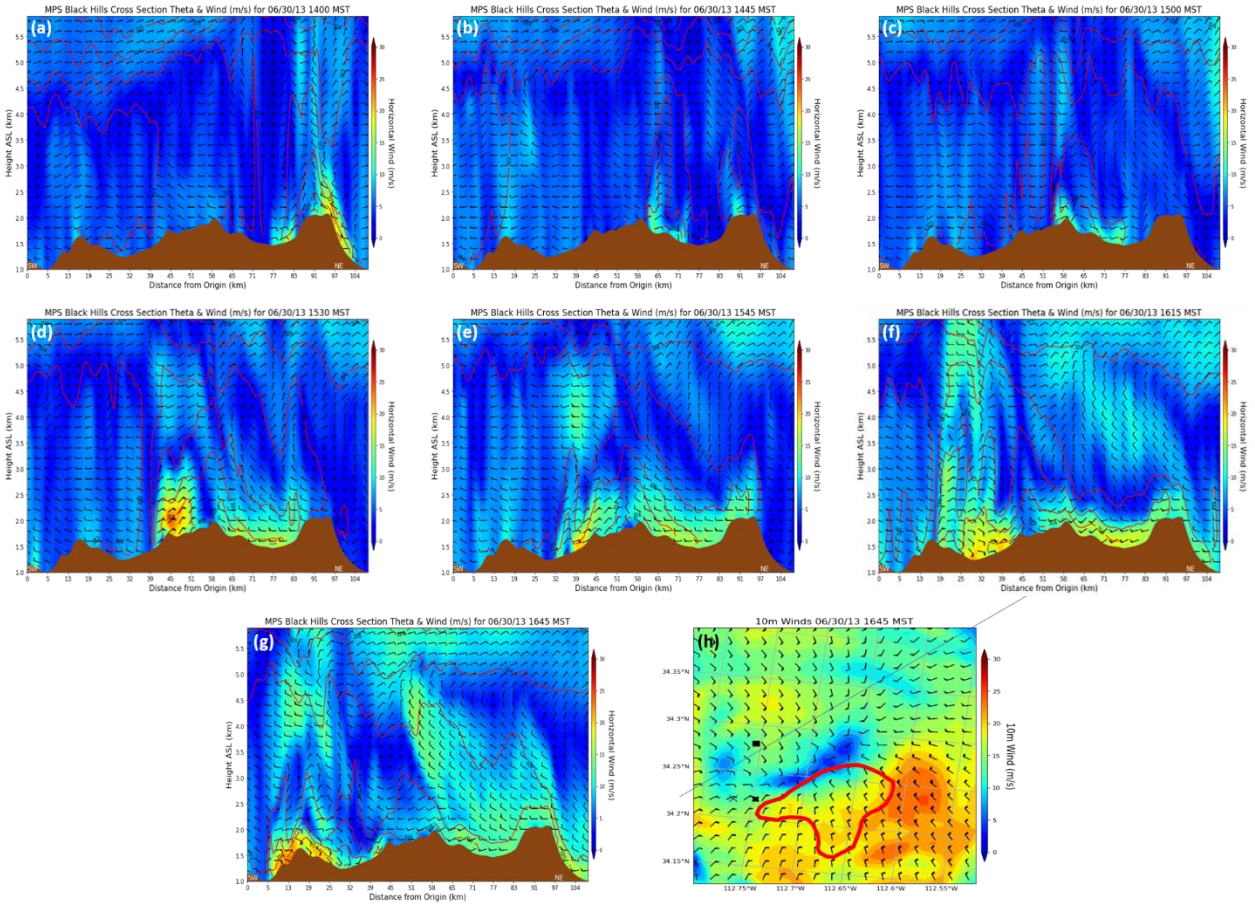

Figure 22. WRF-ARW-simulated 777-m horizontal wind isotachs (fill in m s^{-1}) and barbs (m s^{-1}) and theta (red in K) along the cross-section in Figures 3a and 22a–g extending southwest to northeast. Towards the northeast are the Black Hills, the Bradshaw Mountains are in the center of each figure, and the Weaver Mountains are toward the southwest valid at (**a**) 2100 UTC, (**b**) 2145 UTC, (**c**) 2200 UTC, (**d**) 2230 UTC, (**e**) 2245 UTC, (**f**) 2315 UTC, (**g**) 2345 UTC, and (**h**) horizontal cross-section of the same at 2345 UTC 30 June 2013. In (**h**), red isoline is the Eastern Weaver Mountain perimeter, the solid line is the cross-section in Figure 3b, a dark black x is Yarnell, a light black x at 34.22° N, 112.76° W is the fire fighters' location, and the black square is the incident command post. From [13].

The first group of figures (Figure 22a–g) indicates the continuity of convective density current-induced momentum surges from the Black Hills to the Bradshaw Mountains to the Weaver Mountains during the 21/30–2345/30 period after the initial density current over the MR propagated into the Verde Valley and dissipated. The surges ranged in depth from 0.5 km to 1 km AGL and propagated at speeds generally ranging from 10 ms^{-1} to 20 ms^{-1}. The model is slightly fast, slightly too expansive, and biased northwestwards in terms of the density of convective forcing. The key simulated features are: (1) three density currents launched by the Black Hills: one southeastwards, one northeastwards, and the dominant one southwestwards (Figure 22a) and (2) a continuity of the southwestwards propagating current analogous to radar feature L2 all the way from the Black Hills through the Bradshaw Mountains into Peeples Valley approaching Yarnell (Figure 22b–f) and (3), the shift in airflow in Figure 22g supported by the horizontal cross-section in Figure 22h, indicating an increased easterly–southeasterly flow during the period beginning at 2330 UTC 30 June and lasting through 2345 UTC 30 June, 2013 near Yarnell juxtaposed with the east–northeasterly flow southeast of Yarnell. The wind pattern in Figure 22g indicates a likely microburst outflow caused by new convection along the western slope of the Eastern

Weaver Mountains interacting with the remnants of the southwestward propagating density current between Yarnell and the location of the City of Prescott firefighters (also, note the northwestern part of the red line in Figure 20g). This microburst is consistent with the drier sub-cloud layer, deeper mixed layer, larger DCAPE, and weaker bulk vertical shear in the Weaver Mountains sounding in Figure 18d as compared to the earlier soundings farther northeast in Figure 18a–c. The added momentum from a microburst, in conjunction with the dying L2′s momentum, where virga and light rain were observed, could have produced the strong wind gusts from the east–northeast observed at the Stanton RAWS Station (not shown) and evidenced by the rapid spread of the fire towards the southwest from 2330 UTC 30 June to 2345 UTC 30 June (Figure 2a).

4. Summary and Conclusions

The fundamental sequence of weather events organizing the YHFT can be summarized as follows:

1. The circulation over North America transitioned to a transport of cool arctic air equatorward, creating a meridional temperature gradient across the U.S.–Canadian border.
2. A polar jet streak encounters this meridional temperature gradient across the U.S.–Canadian border causing the primary baroclinic, cyclonic RWB to occur, resulting in equatorward PV transport.
3. Broad trough thinning accompanying the RWB is followed by a weaker secondary anticyclonic RWB, which reinforces the equatorward reversal of the PV maxima aloft.
4. Two short-wave troughs accompanying the RWBs advected cool low-level air from the Central U.S. towards and over the Front Range of the Rocky Mountains, where low-level IW frontogenesis occurs.
5. Low-level moist air was advected by the nocturnal low-level jet into the river valleys of New Mexico and Arizona.
6. A secondary jet streak developed near the low-level IW front and organized a tertiary finer scale jetlet in its unbalanced right entrance region.
7. This jetlet subsequently increased the divergence above the MPS over the MR and adjacent mountains, enhancing the ascent from the low-level thermally direct circulation.
8. This intensifying jetlet resulted in ageostrophy, divergence, vertical wind shear, and ascent between the MR and Yarnell.
9. Convection just north and northeast of Yarnell organized into dual convective lines and a southwestward propagating density current.
10. The density current and its northeasterly winds approached Yarnell through Peeples Valley. It subsequently organized new convection in a less sheared and more unstable environment along the slopes of the Eastern Weaver Mountains, organizing a propagating microburst with outflowing easterly winds converging with the dying density current's northeasterly winds near the firefighters.

A higher resolution WRF 259-m nested-grid simulation is presently being generated to better analyze the local microburst-induced airflow near the firefighters' location, which, in turn, will be employed to initialize WRF-FIRE to diagnose the local fire/atmosphere interactions at the canyon scale.

Author Contributions: Conceptualization, M.L.K., C.N.J., M.R.S. and J.I.; methodology, M.L.K., C.N.J., M.R.S. and J.I.; software: C.N.J., J.I., M.R.S., J.R., S.M.S.K. and J.W.; validation, M.L.K., C.N.J., J.R., J.W. and S.M.S.K.; formal analysis, M.L.K., C.N.J., M.R.S. and J.I.; investigation, M.L.K., C.N.J. and J.I., resources, C.N.J. and Y.-L.L.; data curation, M.R.S., J.R., S.M.S.K. and J.W.; writing—original draft presentation, M.L.K.; writing—review and editing, C.N.J., M.R.S. and A.T.; visualization, C.N.J., J.I., M.R.S., J.R., S.M.S.K. and J.W.; supervision, M.L.K.; project administration, M.L.K., C.N.J. and Y.-L.L.; and funding acquisition, M.L.K. and Y.-L.L. All authors have read and agreed to the published version of the manuscript.

Funding: This research was supported under NSF Grant Subaward #260349A to NSF Awards #1900621 and # 2022961.

Acknowledgments: The authors would like to acknowledge NCAR and the Computational and Information Systems Laboratory (CISL) for their support of computing times on the Cheyenne supercomputer (Project No. UNCS0030). Ronny Schroeder of Embry-Riddle Aeronautical University is acknowledged for assisting us with plotting the fire perimeter map in Figure 2a. Kacie Nicole Shourd is acknowledged for additional reviewing and editing, as well as manuscript formatting.

Conflicts of Interest: The authors declare no conflict of interest. The funders had no role in the design of the study; in the collection, analyses, or interpretation of the data; in the writing of the manuscript; or in the decision to publish the results.

Abbreviations

m = meter, dam = decameter, km = kilometer, s = second, kt = knot, d = day, j = joule, g = gram, kg = kilogram, K = degrees Kelvin temperature, C = degrees Celsius temperature, F = degrees Fahrenheit temperature, hPa = hectopascal, mb = millibar, μb = microbar, CAPE = convective available potential energy, MUCAPE = most unstable convective available potential energy, DCAPE = downdraft convective available potential energy, CIN = convective inhibition, SBCIN = surface-based convective inhibition, dBZ =decibel, ZDR = differential reflectivity, CC = correlation coefficient, PV = potential vorticity, PVU = potential vorticity units, AGL = above ground level, MSL = mean sea level, RWB = Rossby wave breaking, MR = Mogollon Rim, IW = Intermountain West, CP = Colorado Plateau, N = north latitude, W = west latitude, WRF = Weather Research and Forecasting Model, MPS = mountain-plains solenoidal circulation, UTC = universal coordinated time, AZ = Arizona, WRF-ARW = Weather Research and Forecasting-Advanced Research Weather, WRF-Fire = Weather Research and Forecasting-Coupled Wildland Fire Modeling, PJ = polar jet.

References

1. National Weather Service. Yarnell Fire. 28 June–10 July 2013. Available online: https://tinyurl.com/ybsremce (accessed on 3 October 2021).
2. Lafire. The Fire of '33. Available online: http://www.lafire.com/famous_fires/1933-1003_GriffithParkFire/1933-1003_GriffithParkFire.htm (accessed on 3 October 2021).
3. Yarnell Hill Briefing Video. Available online: https://www.youtube.com/watch?v=cSxSqjRmxIE&t=1203s (accessed on 3 October 2021).
4. Aiguo, D.; National Center for Atmospheric Research Staff (Eds.) The Climate Data Guide: Palmer Drought Severity Index (PDSI). Available online: https://climatedataguide.ucar.edu/climate-data/palmer-drought-severity-index-pdsi (accessed on 3 October 2021).
5. Taylor, A.A.; Klimowski, B.A.; Staudenmaier, M.J., Jr. Meteorological Conditions and Decision Support Services Associated with the Yarnell Hill Fire. In Proceedings of the Third Symposium on Building a Weather-Ready Nation: Enhancing Our Nation's Readiness, Responsiveness, and Resilience to High Impact Weather Events, American Meteorological Society 95th Annual Meeting, Phoenix, AZ, USA, 6 January 2015.
6. Maddox, R.A.; McCollum, D.M.; Howard, K.W. Large-scale patterns associated with severe summertime thunderstorms over central Arizona. *Weather. Forecast.* **1995**, *10*, 763–778. [CrossRef]
7. Mazon, J.J.; Castro, C.L.; Adams, D.; Chang, H.-I.; Carrillo, C.M.; Brost, J.J. Objective Climatological Analysis of Extreme Weather Events in Arizona during the North American Monsoon. *J. Appl. Meteorol. Clim.* **2016**, *55*, 2431–2450. [CrossRef]
8. Yang, L.; Smith, J.; Baeck, M.L.; Morin, E. Flash Flooding in Arid/Semiarid Regions: Climatological Analyses of Flood-Producing Storms in Central Arizona during the North American Monsoon. *J. Hydrometeorol.* **2019**, *20*, 1449–1471. [CrossRef]
9. Castro, C.L.; Pielke, R.A.; Adegoke, J.O. Investigation of the Summer Climate of the Contiguous United States and Mexico Using the Regional Atmospheric Modeling System (RAMS). Part I: Model Climatology (1950–2002). *J. Clim.* **2007**, *20*, 3844–3865. [CrossRef]
10. Castro, C.L.; Pielke, R.A.; Adegoke, J.O.; Schubert, S.D.; Pegion, P.J. Investigation of the Summer Climate of the Contiguous United States and Mexico Using the Regional Atmospheric Modeling System (RAMS). Part II: Model Climate Variability. *J. Clim.* **2007**, *20*, 3866–3887. [CrossRef]
11. Castro, C.L.; Chang, H.-I.; Dominguez, F.; Carrillo, C.; Schemm, J.E.; Juang, H.-M.H. Can a Regional Climate Model Improve the Ability to Forecast the North American Monsoon? *J. Clim.* **2012**, *25*, 8212–8237. [CrossRef]
12. Mccollum, D.M.; Maddox, R.A.; Howard, K.W. Case Study of a Severe Mesoscale Convective System in Central Arizona. *Weather Forecast.* **1995**, *10*, 643–665. [CrossRef]

13. Ising, J.; Lin, Y.-L.; Kaplan, M.L. Effects of density current, diurnal heating, and local terrain on the mesoscale environment conducive to the Yarnell Hill Fire. *Meteorol. Atmos. Phys.* **2021**, Submitted.
14. Damiani, R.; Zehnder, J.; Geerts, B.; Demko, J.; Haimov, S.; Petti, J.; Poulos, G.S.; Razdan, A.; Hu, J.; Leuthold, M.; et al. The Cumulus Photogrammetric, In-situ and Doppler Observations Experiment of 2006. *Bull. Am. Meteor. Soc.* **2008**, *89*, 57–73. [CrossRef]
15. Demko, J.C.; Geerts, B.; Miao, Q.; Zehnder, J.A. Boundary Layer Energy Transport and Cumulus Development over a Heated Mountain: An Observational Study. *Mon. Weather Rev.* **2009**, *137*, 447–468. [CrossRef]
16. Carbone, R.E. A Severe Frontal Rainband. Part I. Stormwide Hydrodynamic Structure. *J. Atmos. Sci.* **1982**, *39*, 258–279. [CrossRef]
17. Wakimoto, R.M. The life cycle of thunderstorm gust fronts as viewed with Doppler radar and rawisonde data. *Mon. Weather Rev.* **1982**, *110*, 1060–1082. [CrossRef]
18. Rotunno, R.; Klemp, J.B.; Weisman, M.L. A theory for strong, long-lived squall lines. *J. Atmos. Sci.* **1988**, *45*, 463–485. [CrossRef]
19. Xu, Q.; Moncrieff, M.W. Density current circulations in shear flows. *J. Atmos. Sci.* **1994**, *51*, 434–446. [CrossRef]
20. Liu, C.; Moncrieff, M.W. A Numerical Study of the Effects of Ambient Flow and Shear on Density Currents. *Mon. Weather Rev.* **1996**, *124*, 2282–2303. [CrossRef]
21. Liu, C.; Moncrieff, M.W. An analytical study of density currents in sheared, stratified fluids including the effects of latent heat release. *J. Atmos. Sci.* **1996**, *53*, 3303–3312. [CrossRef]
22. Xue, M.; Xu, Q.; Droegemeier, K.K. A theoretial and numerical study of density currents in nonconstant shear flows. *J. Atmos. Sci.* **1997**, *54*, 1998–2019. [CrossRef]
23. Moncrieff, M.W.; Liu, C. Convection initiation by density currents: Role of convergence, shear, and dynamical organization. *Mon. Weather Rev.* **1999**, *127*, 2455–2464. [CrossRef]
24. Plymouth State Weather Center. Available online: https://vortex.plymouth.edu/ (accessed on 3 October 2021).
25. ECMWF ERA-Interim. Available online: https://www.ecmwf.int/en/forecasts/datasets/reanalysis-datasets/era-interim (accessed on 3 October 2021).
26. ECMWF ERA5. Available online: https://www.ecmwf.int/en/forecasts/datasets/reanalysis-datasets/era5 (accessed on 3 October 2021).
27. NOAA NCEI NEXRAD Data Archive, Inventory and Access. Available online: https://www.ncdc.noaa.gov/nexradinv (accessed on 3 October 2021).
28. NWS Forecast Office Flagstaff, AZ. Available online: https://www.weather.gov/fgz/ (accessed on 3 October 2021).
29. Durre, I.; Xungang, Y.; Vose, R.S.; Applequist, S.; Arnfield, J. *Integrated Global Radiosonde Archive (IGRA), Version 2*; National Centers for Environmental Information (NCEI): Asheville, NC, USA, 2016. [CrossRef]
30. Remote Automatic Weather Stations (RAWS). Available online: https://raws.nifc.gov/ (accessed on 3 October 2021).
31. Sinclair, M.R. Use of a simple graphics viewer for gridded data to improve data literacy. In Proceedings of the 24th Symposium on Education American Meteorological Society, Phoenix, AZ, USA, 4–8 January 2015.
32. Skamarock, W.C.; Klemp, J.B.; Dudhia, J.; Gill, D.O.; Barker, D.M.; Wang, W.; Powers, J.G. *A Description of the Advanced Research WRF Version 2*; NCAR Technical Note NCAR/TN–468+STR; National Center for Atmospheric Research: Boulder, CO, USA, 2005; p. 100.
33. Grell, G.A.; Freitas, S.R. A scale and aerosol aware stochastic convective parameterization for weather and air quality modeling. *Atmos. Chem. Phys.* **2014**, *14*, 5233–5250. [CrossRef]
34. Mielikainen, J.; Huang, B.; Huang, H.L.A. Optimizing the Purdue-Lin microphysics scheme for Intel Xeon Phi Coprocessor. *IEEE J. Sel. Top. Appl. Earth Obs. Remote Sens.* **2016**, *9*, 425–438. [CrossRef]
35. Mellor, G.L.; Yamada, T. A Hierarchy of Turbulence Closure Models for Planetary Boundary Layers. *J. Atmos. Sci.* **1974**, *31*, 1791–1806. [CrossRef]
36. Janjic, Z.I. The step-mountain eta coordinate model: Further developments of the convection, viscous sublayer, and turbulence closure schemes. *Mon. Weather Rev.* **1994**, *122*, 927–945. [CrossRef]
37. Janjic, Z. Nonsingular Implementation of the Mellor-Yamada Level 2.5 Scheme in the NCEP Meso model. *NCEP Off. Note* **2002**, *437*, 61.
38. Chen, F.; Dudhia, J. Coupling an Advanced Land Surface–Hydrology Model with the Penn State–NCAR MM5 Modeling System. Part I: Model Implementation and Sensitivity. *Mon. Weather Rev.* **2001**, *129*, 569–585. [CrossRef]
39. Ek, M.B.; Mitchell, K.E.; Lin, Y.; Rogers, E.; Grunmann, P.; Koren, V.; Gayno, G.; Tarpley, J.D. Implementation of Noah land surface model advances in the National Centers for Environmental Prediction operational mesoscale Eta model. *J. Geophys. Res. Space Phys.* **2003**, *108*, 8851. [CrossRef]
40. Dudhia, J. Numerical Study of Convection Observed during the Winter Monsoon Experiment Using a Mesoscale Two-Dimensional Model. *J. Atmos. Sci.* **1989**, *46*, 3077–3107. [CrossRef]
41. Mlawer, E.J.; Taubman, S.J.; Brown, P.D.; Iacono, M.J.; Clough, S.A. Radiative transfer for inhomogeneous atmospheres: RRTM, a validated correlated-k model for the longwave. *J. Geophys. Res. Atmos.* **1997**, *102*, 16663–16682. [CrossRef]
42. May, R.M.; Arms, S.C.; Marsh, P.; Bruning, E.; Leeman, J.R.; Goebbert, K.; Thielen, J.E.; Bruick, Z. MetPy: A Python Package for Meteorological Data. *Unidata* **2021**. Available online: https://github.com/Unidata/MetPy (accessed on 3 October 2021). [CrossRef]

43. Postel, G.A.; Hitchman, M.H. A climatology of Rossby wave breaking along the subtropical tropopause. *J. Atmos. Sci.* **1999**, *56*, 359–373. [CrossRef]
44. Abatzoglou, J.T.; Magnusdottir, G. Planetary wave breaking and nonlinear reflection: Seasonal cycle and interannual variability. *J. Clim.* **2006**, *19*, 6139–6152. [CrossRef]
45. Kaplan, M.L.; Tilley, J.S.; Hatchett, B.J.; Smith, C.M.; Walston, J.M.; Shourd, K.N.; Lewis, J.M. The Record Los Angeles Heat Event of September 2010: 1. Synoptic-Scale-Meso-β-Scale Analyses of Interactive Planetary Wave Breaking, Terrain- and Coastal-Induced Circulations. *J. Geophys. Res. Atmos.* **2017**, *122*, 710–729. [CrossRef]
46. Mecikalski, J.R.; Tilley, J.S. Front Range Cold Surges: Development of a Classification Scheme. *Meteor. Atmos. Phys.* **1992**, *48*, 249–271. [CrossRef]
47. Kaplan, M.L.; Koch, S.E.; Lin, Y.L.; Weglarz, R.P.; Rozumalski, R.A. Numerical simulations of a gravity wave event over CCOPE. Part I: The role of geostrophic adjustment in mesoscale ageostrophic jetlet formation. *Mon. Weather Rev.* **1997**, *125*, 1185–1211. [CrossRef]
48. Hamilton, D.W.; Lin, Y.L.; Weglarz, R.P.; Kaplan, M.L. Jetlet formation with diabatic forcing with applications to the 1994 Palm Sunday tornado outbreak. *Mon. Weather Rev.* **1998**, *126*, 2061–2089. [CrossRef]
49. Koch, S.E.; Hamilton, D.; Kramer, D.; Langmaid, A. Mesoscale dynamics in the Palm Sunday tornado outbreak. *Mon. Weather Rev.* **1998**, *126*, 2031–2060. [CrossRef]
50. Lin, Y.-L. *Mesoscale Dynamics*; Cambridge University Press: Cambridge, UK, 2010; p. 646. ISBN 13978-0521004848.
51. Uccellini, L.W.; Koch, S.E. The synoptic setting and possible energy sources for mesoscale wave disturbances. *Mon. Weather Rev.* **1987**, *115*, 721–729. [CrossRef]
52. Banta, R.M. Daytime boundary-layer evolution over mountainous terrain. Part I: Observations of the dry circulations. *Mon. Weather Rev.* **1984**, *112*, 340–356. [CrossRef]
53. Tripoli, G.J.; Cotton, W.R. Numerical study of an observed orogenic mesoscale convective system. Part I: Simulated genesis and comparison with observations. *Mon. Weather Rev.* **1989**, *117*, 273–304. [CrossRef]
54. Melnikov, V.M.; Zrnic, D.S.; Rabin, R.M.; Zhang, P. Radar polarimetric signatures of fire plumes in Oklahoma. *Geophys. Res. Lett.* **2008**, *35*, L14815. [CrossRef]